1. Introduction

Mass loss phenomena in the form of powerful bipolar jets and molecular outflows are often associated with the early evolution of protostars. Together with indirectly regulating the accretion process, they play a crucial rôle also in the interaction between the protostar and the natal environment, causing injection of momentum, kinetic energy and turbulence in the ISM, along with irreversible modifications of its chemical structure and physical conditions. The most violent interaction occurs at the terminal working surface, where the supersonic flow impacts the undisturbed medium and most of the ambient material is entrained by the jet (e.g. Reipurth & Bally, 2001). In a schematic model, the interaction occurs via two shocks: an internal working surface (Mach disk) which decelerates the jet gas and a forward shock which accelerates the ambient gas producing a mixture of shock velocities (e.g. Hartigan, 1989). This latter has often a curve-shaped morphology: therefore, only the component of motion along the jet axis is slowed going from the apex of the shock toward the receding parts, where large transverse motions occur. In a classical scenario, for sufficiently fast shocks, the head of the bow is a pure dissociative (J)ump-type shock (Hollenbach & McKee, 1989), which changes along the bow flanks, where the impact occurs obliquely, to slower, non-dissociative (C)ontinuos-type shocks (Draine, 1980). In this framework, highly excited ionic emission should arise at the head of the bow, while molecular emission mainly originates from the cooling regions along the flanks and behind the bow. Recent models, however, predict that mixtures of J- and C-type shocks can occur along the overall structure of the bow, or, in the presence of a sufficiently strong magnetic field, that a J-type shock can evolve into a C-type, remaining embedded at early time (Smith & Rosen, 2003; Smith & Mac Low, 1997; Flower et al., 2003; Le Bourlot et al., 2002, Lesaffre et al., 2004a,b).

The large number of parameters which regulate the shock physics (e.g. strength and direction of the local magnetic field, ionisation fraction and density gradient between the shocked gas and the local environment) can be constrained only through dedicated observations aimed at probing the physical and kinematical properties of the gas all along the bow structure. In this respect, observations in the near-infrared represent a well suited tool: both H_2 ro-vibrational lines, which are the main gas coolants in continuos shock components, and fine structure transitions of abundant atomic species (e.g. Fe II, C I, S II), which are expected to emit in dissociative shocks, fall in this wavelength range. Indeed, in recent years multiple observations of jets and bow shocks have been conducted in the near-infrared by means of long-slit spectroscopy (e.g. Eislöffel, Smith & Davis, 2000; Giannini et al., 2004; Smith, Froebrich & Eislöffel, 2003; Nisini et al., 2002; O'Connell, Smith & Davis, 2004; Nisini et al., 2005). The observed spectra are typically rich in both molecular (H_2) and ionic ([FeII]) lines, implying that strong gradients in the local conditions (e.g. temperature, fractional ionisation) do occur and that multiple shock components are simultaneously at work. The main limitation of long-slit spectroscopy for studying in detail bow-shock morphologies arises from the poor coverage of the extended bow surface usually obtainable in a reasonable amount of observing time; on the contrary, Integral Field Spectroscopy (IFU) represents a well-tailored tool to overcome this problem, since it allows us to obtain simultaneously 2-D maps at different wavelengths. In this paper we present the spectral images obtained with the IFU facility SINFONI (Eisenhauer et al., 2003, Bonnet et al., 2004) of a prototype bow-shock, namely the Herbig-Haro object HH99B. This is located in the RCrA molecular core at d∼ 130 pc (Marraco & Rydgren, 1981), and it was firstly discovered in the optical by Hartigan & Graham (1987), who suggested it is the red-shifted lobe of the outflow powered by the HH100-IR source. More recently, Wilking et al.(1997) have proposed, on the basis of near-infrared images, the infrared source IRS9 and the Herbig Ae star RCrA as other possible exciting source candidates. HH99B was firstly imaged in the near-infrared by Davis et al. (1999, hereafter D99) who identified three different emission zones: one at the head of the bow (subsequently named B0 by McCoey et al., 2004, hereafter MC04) where the bulk of the emission comes from ionised gas, and two bow-flanks (knots B1 and B3), which emit mainly in H_2 lines. A further H_2 knot, immediately behind the bow apex, was identified as knot B2. In the framework of both bow- (D99) and planar- (MC04) shock models, some attempt has been made to model the line emission observed in HH99B: the H_2 morphology is well fitted by a C-type bow shock, while the physical conditions of the molecular gas (measured by means of long-slit spectroscopy) have been accounted for by a planar J-type shock with a magnetic precursor. None of these two models, however, is able to reproduce the copious ionic emission, that requires the presence of a further fully dissociative shock component.

With the present work we aim at putting strong observational constraints on bow-shock models. (whose detailed application will be subject of a separated paper). In particular we intend to: *(i)* morphologically characterise the emission of the different lines; *(i)* derive maps of the main physical parameters which govern the shock physics; *(iii)* study the velocity field(s) along the bow structure.

Our work is organised as follows: Section 2 describes our observations and the obtained results; the line excitation analysis and the kinematical properties are then presented in Sections 3 and 4. Concluding remarks are given in Section 5, while in Appendix A we describe the procedure we have applied to derive the inclination angle of HH99B.

2. Observations and Results

HH99B was observed during four different runs in May and July 2006 with the SINFONI-SPIFFI instrument at the VLT-UT4 (ESO Paranal, Chile). The coordinates of the pointed position are: $\alpha_{2000}=19^h02^m05.4^s$, $\delta_{2000}=-36°54'39''$. The Integral Field Unit was employed to obtain spectroscopic data in J (1.10-1.40 μm), H (1.45-1.85 μm) and K (1.95-2.45 μm) bands, at spectral resolution 2000, 3000, and 4000, respectively, each wavelength band fitting on the 2048 pixels of the Hawaii detector in the dispersion direction. An image slicer converts the bidimensional field-of-view into a one-dimensional long-slit, that is fed into a spectrograph to disperse the light of each pixel simultaneously. As a consequence seeing and atmospheric response can affect neither the emission morphology at a given wavelength nor intensity ratios of

lines within the same filter. The spatial resolution was selected at $0.25''$ per image slice, which corresponds to a field-of-view of $8'' \times 8''$. No adaptive optics is supported in this configuration. The total integration time is 2400 s, 1500 s, and 1800 s in J, H, and K bands, respectively. The observations were acquired by nodding the telescope in the usual ABB$'$A$'$ mode and a telluric B-type standard star close to the source was observed to remove the atmospheric spectral response.

The SINFONI data reduction pipeline (Modigliani, Ballester & Peron, 2007) has been used to subtract the sky emission, to construct dark and bad pixel maps and flat field images, to correct for optical distorsions and to measure wavelength calibration by means of Xenon-Argon lamp images. Further analysis has been carried out with IRAF packages and IDL scripts, that were used to remove telluric absorption features: this task was accomplished by dividing the target images by those of the telluric standard star, once corrected for both the stellar continuum shape (a black-body function at the stellar temperature) and its intrinsic absorption features (mainly hydrogen recombination lines). Photometric calibration was obtained from the same standard star. Since there is not overlapping in the spectral range covered by the different grisms, no cross-calibration has been performed at this step of the data reduction. However, we have checked *a posteriori* the reliability of our absolute fluxes once an extinction map for the H_2 line emission has been obtained (Sect.3.1.2): we have measured the departure from the theoretical value in the image ratio of de-reddened lines coming from the same level and lying in different spectral bands. In this way we estimate a cross-calibration better than 5% between J and H bands, and than 12% between H and K bands. Atmospheric OH lines were also used to refine wavelength calibration and to measure the effective spectral resolution: we obtain $R \sim 1900$, 2700, 3500 in J, H, and K bands, that correspond to 160, 110, 85 km s^{-1}, respectively. At these spectral resolutions we are able to resolve the brightest lines (e.g. H_2 2.122μm and [Fe II] 1.644μm), which are observed at S/N ratios of $\sim 10^2$-10^3. As a final step, images of lines observed in individual bands ([Fe II]1.257μm and 1.644μm in the J and H bands and H_2 2.122μm in the K band) were used to re-align the images acquired in different observing runs.
As a result, we obtained a 3D data-cube containing the HH99B image in more than 170 lines.[1] As an example of our results, we have integrated the signal in the areas corresponding to knots B0 and B3 (see Figure 1): the corresponding spectra are shown in Figures 2-4. The large majority of the detected lines are H_2 ro-vibrational lines (121). For these, we list in Table 1 spectral identification, vacuum wavelength, excitation energy (in K) and the maximum S/N ratio registered in the corresponding image. The detected ro-vibrational transitions come from levels with $v \leq 7$ and E_{up} up to $\sim 38\,000$ K, many of them never observed before in HH objects. In particular, as we show in Figure 1 (upper panel), emission of lines with $E_{up} \lesssim 30\,000$ K is present only along the bow flanks, while lines with $E_{up} \gtrsim 30\,000$ K are observed in the whole shock, peaking at the bow head. Therefore, two main results emerge: *(i)* molec-

---

ular hydrogen survives also where ionic emission is strong (see below) and, *(ii)* temperature gradients do exist along the shock, with the highest values reached at the bow head, where stronger excitation conditions are expected to occur. Atomic lines are listed in Table 2 and some examples of the observations are shown in Figure 1, middle and bottom panels. Plenty of [Fe II] lines are detected (34 lines), emitted from levels with $E_{up} \lesssim 30\,000$ K. As for H_2, two groups of lines are identified: those with $E_{up} \lesssim 13\,000$ K, which come for the a^{4}D level, are observed in the whole region, while those at higher excitation energy are emitted only at the bow head. In this same area, emission of hydrogen and helium recombination lines (8 and 3 lines, respectively, see Figure 1, bottom panel) along with fine structure lines of [P II],[Co II], and [Ti II] are detected. Other fine structure lines commonly observed in Herbig-Haro objects (e.g. [C I] at 0.98μm, [N I] at 1.04μm, [S II] at 1.03μm, Nisini et al., 2002) are not covered with SINFONI. In fact, the first wavelength in the J band is λ=1.10μm, i.e. longer than that of other infrared spectrographs (e.g. ISAAC and SofI at ESO are able to observe wavelengths longer than 0.98μm and 0.86μm, respectively).

To check for possible line variability, the intensities of atomic and molecular lines observed with SINFONI were compared with the ones observed by MC04 in July 2002 (i.e. four years before our SINFONI observations). Synthetic slits corresponding to slit 1 and 2 of MC04 (PA=32.4° and 329.5°, width 0.6$''$) were superimposed onto the SINFONI images and the flux was integrated over the same regions as in that paper. The main difference between SINFONI and ISAAC spectra is represented by the significant larger number of lines observed with SINFONI (see Figures 2-4 and Figure 3 and Table 1 of MC04). In particular, it is noticeable the detection of many lines at high excitation, both atomic and molecular, that indicate excitation conditions stronger than those inferred in that paper (see Table 3). A general increase in the intensities of lines observed with both the instruments is registered, but with differential behaviour among molecular and ionic lines, which are respectively 4 and 1.5 times brighter than four years before. Such variability has been observed in proper motion studies, over time periods of a few years typical of radiative cooling times in HH objects (e.g. Caratti o Garatti et al., 2008).

## 3. Diagnostics of physical parameters

3.1. Fe analysis

3.1.1. On [Fe II] Einstein coefficients

In Table 2 the [Fe II] lines are listed grouping transitions originating from the same upper level. The intensity ratio of pairs of (optically thin) lines in each group is independent of the local physical conditions, being function only of atomic parameters (i.e. line frequencies and Einstein A coefficients for spontaneous emission). Hence, the *observed* intensity ratios among these lines can be efficiently used to measure the local extinction (e.g. Gredel, 1994). Unfortunately, the complexity of the energy level system of iron makes very difficult to accurately compute the A values, so that three distinct sets of these parameters, differing by more than 30%, have been sofar listed in the literature: two were computed with different methods by Quinet, Le Dourneuf & Zeippen, (Q-SST, Q-HFR, 1996), and one is provided by
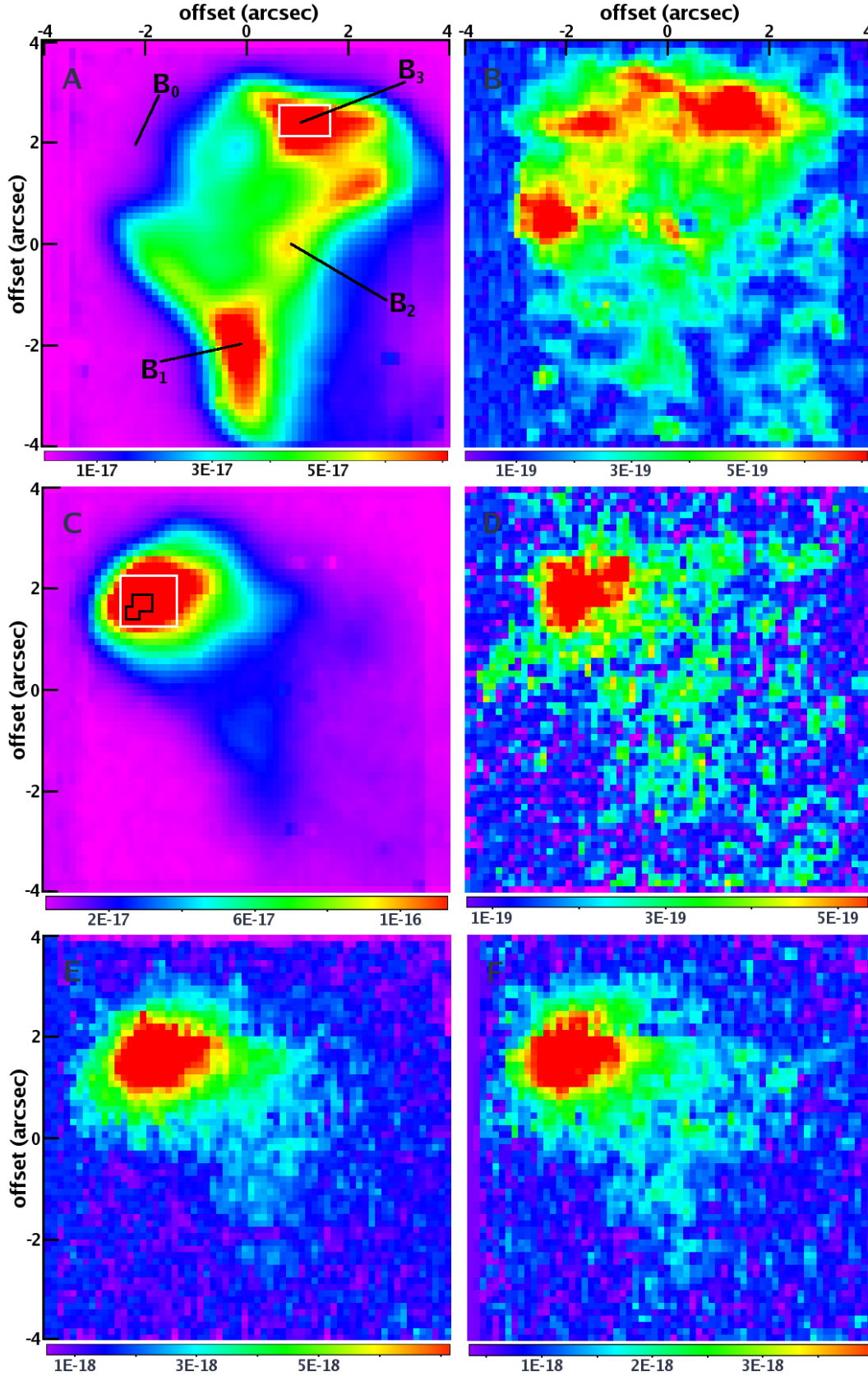
Fig. 1. Selected spectral images from our HH99B data-cube. Intensities are given in colour scale. Offsets are from $\alpha_{2000}=19^h02^m05.4^s$, $\delta_{2000}=-36°54'39''$. A) H_2:1-0 S(1) at 2.122μm. The locations of the knots labelled by D99 (B1, B2 and B3) and MC04 (B0) are indicated; B) H_2: 2-1S(17) at 1.758μm; C) [Fe II]: $a^4D_{7/2}$-$a^4F_{9/2}$ at 1.644μm. The black line delimits the area where [Fe II] lines at S/N > 100 are detected and used to construct the plot of Figure 5; D) [Fe II]: $a^4P_{3/2}$-$a^4D_{7/2}$ at 1.749μm; E) H:Paβ at 1.282μm; F) [P II]: $^2D_2$-$^3P_2$ at 1.188μm. White rectangles in panels A) and C) indicate the areas over which we have integrated the signal and extracted the spectra shown in Figures 2-4.
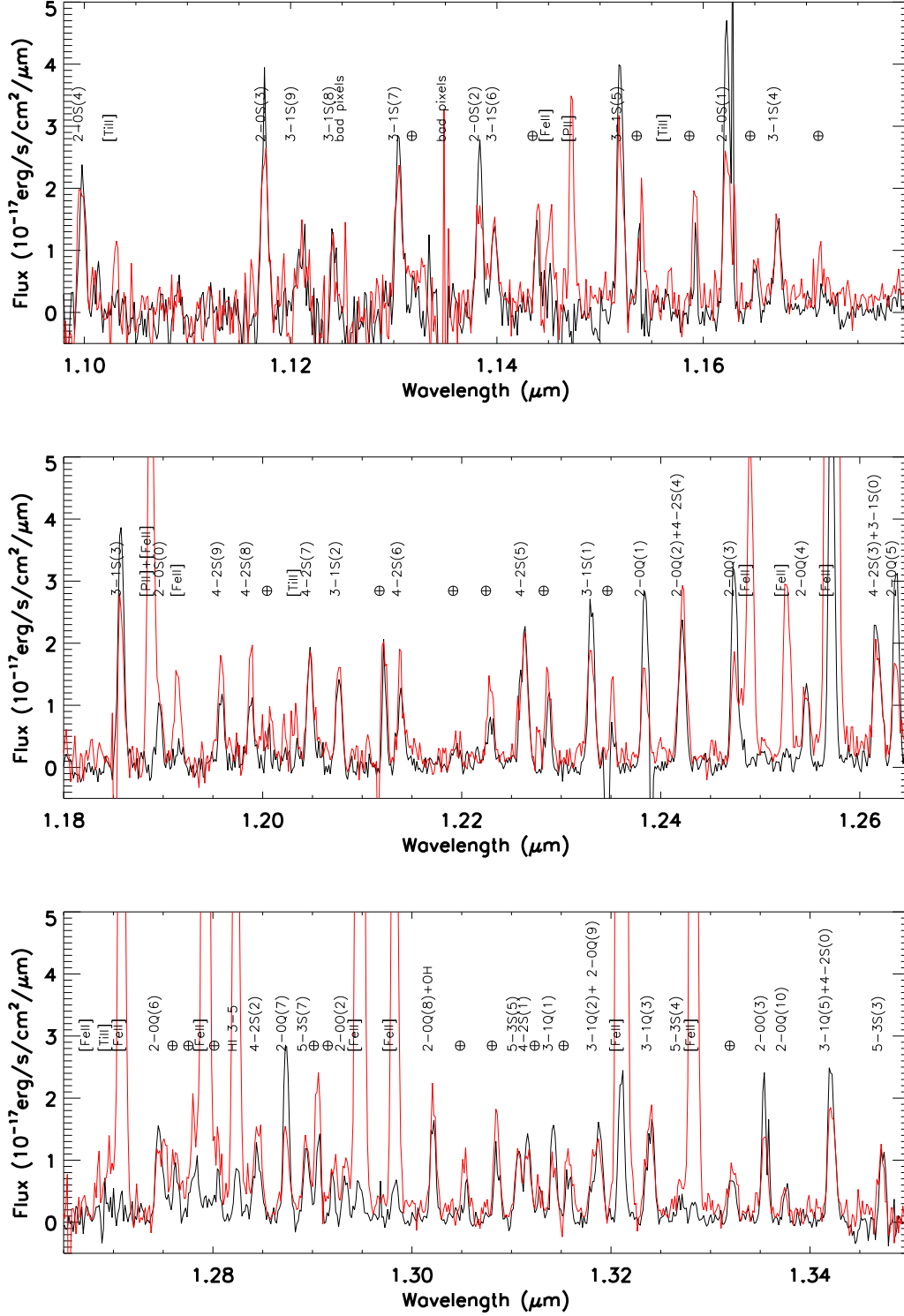
Fig. 2. J band spectrum extracted in knot B3 (black) and B0 (red), over an area of 0.5 and 1.25 arcsec^2, respectively.

Nussbaumer & Storey (NS, 1988). A fourth list, based on the observation of P Cygni, was recently published by Smith & Hartigan (SH, 2006) who find A values 10%-40% higher than theoretical computations. The application of one set rather than another can lead to significant differences in the derivation of the local extinction. For example, the NS coefficients of the 1.644μm and 1.257μm lines (both coming from the level a$^4D_{7/2}$ with E$_{up}$=11446 K and more commonly observed) provide an extinction 2.7 mag higher than that derivable from the Q-SST coefficients. This marginally affects the NIR lines (the intensity grows by a factor of 2.8 for a line at 1μm and a by factor of 1.4 for a line at 2μm), but becomes critical at optical wavelengths (the intensity grows by a factor of 33.6 at 0.5μm).
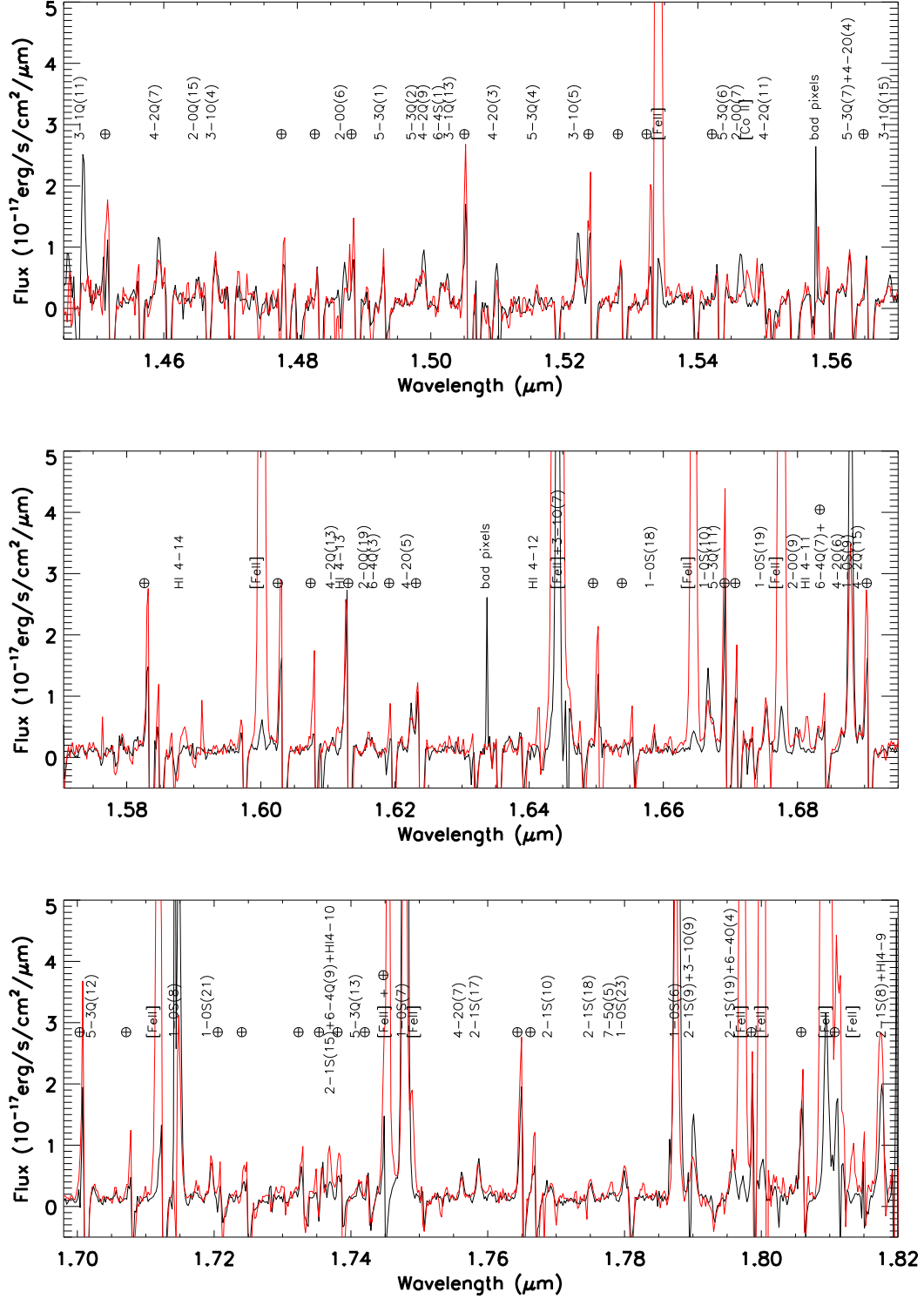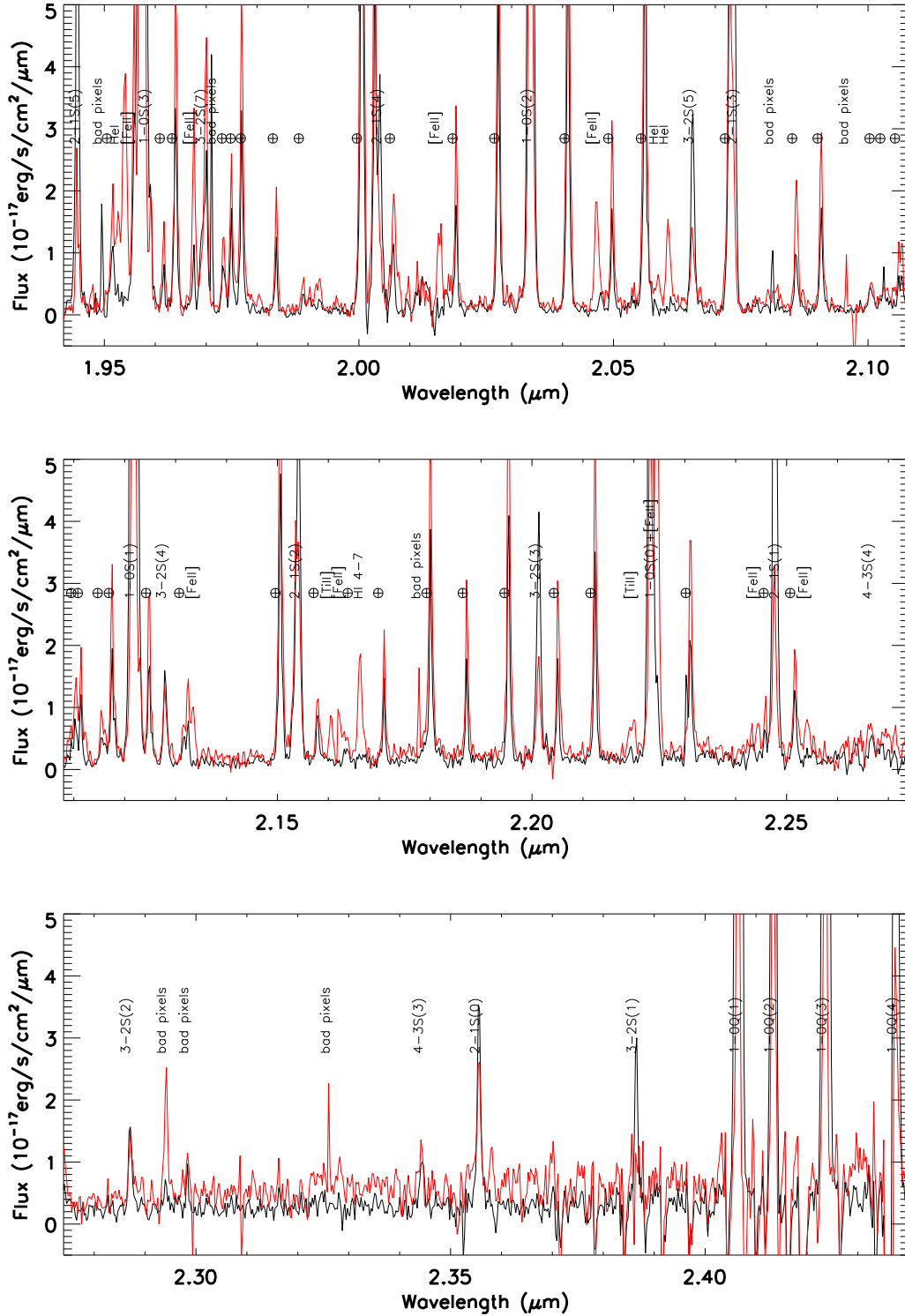
Fig. 3. As in Figure 2 for the H band.

The large number of [Fe II] lines detected in HH99B, observed with a high S/N ratio in a remarkably large fraction of pixels, offers us the opportunity to compare theoretical predictions on the spontaneous emission rates with a significant sample of observational points.

To this aim, we have plotted in Figure 5 the ratios I(1.257μm)/I(1.644μm) vs. I(1.321μm)/I(1.644μm), since these are observed at very high S/N (larger than 100, red

filled squares). In the same Figure, green dashed curves represent the Rieke & Lebofsky (1985) extinction law[2] applied

---

[2] The following arguments remain valid if other extinction laws are adopted (e.g. Cardelli, Clayton & Mathis, 1988), since these do not appreciably differ from the Rieke & Lebofsky law over the short wavelength range taken into consideration (from 1.257μm to 1.644 μm).

Fig. 4. As in Figure 2 for the K band.

to the intrinsic ratios expected for the four sets of A coefficients (Q-SST, Q-HFR, NS, and SH). Squares along these 'extinction curves' indicate $A_V = 0, 5, 10$ mag.

First of all, we note that all the HH99B data lie definitively to the right of any of the plotted extinction curves. Since different A_V can move the points only *along* extinction vectors, no theoretical intrinsic ratio is consistent with the observed points. This result was already pointed out in Nisini et al. (2005), who discussed how the extinction along the knots of the HH1 jet determined from the 1.321μm/1.644μm ratio is always smaller than that derived from the 1.257μm/1.644μm ratio, irrespective of the adopted theoretical set of A coefficients. HH99B data are also inconsistent with the P Cygni datum (green triangle in Figure 5), and consequently with the A coefficients extrapolated from it.

Table 1. H_2 lines observed in HH99B *(to be continued)*.

Line id.	λ_{vac} (μm)	E_{up} (K)	S/N$_{max}^a$	Line id.	λ_{vac} (μm)	E_{up} (K)	S/N$_{max}$	Line id.	λ_{vac} (μm)	E_{up} (K)	S/N$_{max}$
					H_2 lines						
					$v=1$						
1-0S(0)[1]	2.2233	6471	44	1-0S(7)	1.7480	12818	65	1-0S(21)[3]	1.7195	38136	7
1-0S(1)	2.1218	6951	650	1-0S(8)	1.7147	14221	70	1-0S(23)	1.7801	42122	4
1-0S(2)	2.0338	7584	48	1-0S(9)	1.6877	15723	46	1-0Q(1)	2.4066	6149	44
1-0S(3)	1.9576	8365	46	1-0S(10)	1.6665	17312	9	1-0Q(2)	2.4134	6471	30
1-0S(5)[2]	1.8358	10342	5	1-0S(18)[3]	1.6586	32136	3	1-0Q(3)	2.4237	6951	50
1-0S(6)	1.7879	11522	30	1-0S(19)[3]	1.6750	34131	8	1-0Q(4)	2.4375	7584	18
					$v=2$						
2-0S(0)	1.1896	12095	6	2-0Q(8)	1.3020	16881	9	2-1S(1)	2.2477	12551	44
2-0S(1)	1.1622	12551	48	2-0Q(9)[5]	1.3188	18108	12	2-1S(2)	2.1542	13151	22
2-0S(2)	1.1382	13151	7	2-0Q(10)	1.3375	19436	3	2-1S(3)	2.0735	13891	40
2-0S(3)	1.1175	13891	6	2-0Q(15)	1.4648	27267	3	2-1S(4)	2.0041	14764	21
2-0S(4)	1.0998	14764	6	2-0Q(19)[3]	1.6156	34447	3	2-1S(5)	1.9448	15764	30
2-0Q(1)	1.2383	11790	14	2-0O(2)	1.2932	11636	7	2-1S(8)[6]	1.8183	19435	7
2-0Q(2)[4]	1.2419	12095	9	2-0O(3)	1.3354	11790	16	2-1S(9)[7]	1.7904	20855	22
2-0Q(3)	1.2473	12551	22	2-0O(6)	1.4870	13151	5	2-1S(10)	1.7688	22356	3
2-0Q(4)	1.2545	13151	7	2-0O(7)	1.5464	13891	8	2-1S(15)[8]	1.7387	30794	6
2-0Q(5)	1.2636	13891	11	2-0O(9)	1.6796	15764	5	2-1S(17)[3]	1.7587	34446	4
2-0Q(6)	1.2745	14764	7	2-0O(11)	1.8349	18108	3	2-1S(18)[3]	1.7753	36301	3
2-0Q(7)	1.2873	15764	9	2-1S(0)	2.3556	12095	10	2-1S(19)[3,9]	1.7962	38166	8
					$v=3$						
3-1S(0)[10]	1.2621	17388	9	3-1S(9)	1.1204	25661	22	3-1O(5)	1.5220	17819	10
3-1S(1)	1.2330	17819	10	3-1Q(1)	1.3141	17099	8	3-1O(7)[14]	1.6453	19087	9
3-1S(2)	1.2077	18387	8	3-1Q(2)[12]	1.3181	17388	12	3-1O(9)[11]	1.7898	25661	10
3-1S(3)	1.1857	19087	9	3-1Q(3)	1.3240	17819	8	3-2S(1)	2.3864	17819	8
3-1S(4)	1.1672	19913	8	3-1Q(5)[13]	1.3420	19087	9	3-2S(2)	2.2870	18387	9
3-1S(5)	1.1520	20857	10	3-1Q(11)	1.4479	25661	8	3-2S(3)	2.2014	19087	25
3-1S(6)	1.1397	21912	5	3-1Q(13)	1.5024	28558	6	3-2S(4)	2.1280	19913	11
3-1S(7)	1.1304	23071	7	3-1Q(15)[3]	1.5685	31691	6	3-2S(5)	2.0656	20857	17
3-1S(8)	1.1241	24323	5	3-1O(4)	1.4677	17388	6	3-2S(7)	1.9692	23071	14

To be confident of the reliability of our data, we have checked for possible blendings of the [Fe II] lines with other lines or telluric features. In this respect, the 1.644μm line is close to both the H_2 line 3-1O(7) at 1.6453μm (see Table 1 and Figure 3) and a telluric OH feature at 1.6442μm (Lidman & Cuby, 2000). This latter has been removed in the sky subtraction procedure, and its residuals have been estimated to affect the 1.644μm flux by less than 0.5%. The H_2 line, coming from a low excitation level ($E_{up} \sim 19000$ K), is observed only in the receding parts of the bow, and thus it results *spatially* separated from the 1.644μm emission region.

To check for other observational or data-reduction biases (e.g. unfavourable observational conditions, flat-fielding, intercalibration of lines lying in different bands), we searched in the literature for other observations of the considered lines obtained with other instruments. To minimise the uncertainties, we have considered only line ratios observed with S/N $\geq$ 30, that are shown with different colours/symbols in Figure 5. Notably, all of them occupy the right side of the plot, in agreement with the HH99B points. This result, that reinforces the reliability of our observations, allows us to derive new A coefficients from our observations, provided that these are accurately cor-

rected for the visual extinction value (measured independently from [Fe II] lines). In this respect, two facts have to be noted: *(i)* although the sky area considered for this analysis is a few arcsec^2 (marked in black in Figure 1, middle left panel), an extinction gradient of $\sim$ 1 mag occurs in this zone, as evidenced by the scatter among the data points (red squares) of Figure 5; *(ii)* in the same area, we are able to obtain just a gross estimate of A_V (1.8±1.9 mag) from the observed Pα/Brγ ratio (see Sect. 3.3). Both these circumstances prevent us from deriving an accurate measure of the A ratios. A rough estimate can be however obtained de-reddening the average of the HH99B data (black cross) for $A_V = 1.8$ mag, which gives $A_{1.321}/A_{1.644}$ = 0.38 and $A_{1.257}/A_{1.644}$ = 1.24. The main uncertainty on these values comes, more than from the error on the line fluxes, from the A_V estimate. Taking into account the A_V error of 1.9 mag, we can state that the theoretical points do belong to the segment of the extinction curve (along which they are constrained to move) starting at the point [0.33,1.02] ($A_V = 0$ mag) and ending at the point [0.44,1.48] ($A_V = 3.7$ mag) .

In conclusion, from a pure observational point of view, we can summarise as follows: *(i)* all the theoretically derived A values fail to reproduce the large majority of the

Table 1. H$_2$ lines observed in HH99B *(continued)*.

Line id.	λ_{vac} (μm)	E_{up} (K)	S/N$_{max}^a$	Line id.	λ_{vac} (μm)	E_{up} (K)	S/N$_{max}$	Line id.	λ_{vac} (μm)	E_{up} (K)	S/N$_{max}$
v=4											
4-2S(0)[15]	1.3425	22354	9	4-2S(8)	1.1987	28885	7	4-2O(4)[18]	1.5635	22354	6
4-2S(1)	1.3116	22760	14	4-2S(9)	1.1958	30141	6	4-2O(5)	1.6223	22760	7
4-2S(2)	1.2846	23296	21	4-2Q(7)	1.4592	25625	6	4-2O(6)	1.6865	23297	4
4-2S(3)[16]	1.2615	23956	9	4-2Q(9)	1.4989	27708	7	4-2O(7)	1.7563	23956	7
4-2S(4)[17]	1.2422	24735	9	4-2Q(11)[3]	1.5495	30141	3	4-3S(3)	2.3445	23956	6
4-2S(5)	1.2263	25625	12	4-2Q(13)[3]	1.6123	32857	6	4-3S(4)	2.2667	24735	3
4-2S(6)	1.2139	26618	5	4-2Q(15)[3]	1.6892	35786	6				
4-2S(7)	1.2047	27708	10	4-2O(3)	1.5099	22081	6				
v=5											
5-3S(3)	1.3472	28500	4	5-3Q(1)	1.4929	26737	3	5-3Q(7)[3,19]	1.5626	30065	6
5-3S(4)	1.3270	29231	3	5-3Q(2)	1.4980	26994	9	5-3Q(11)[3]	1.6673	34291	4
5-3S(5)	1.3107[3]	30066	4	5-3Q(4)	1.5158	27880	5	5-3Q(12)[3]	1.7021	35529	4
5-3S(7)	1.2894[3]	32017	7	5-3Q(6)	1.5443	29230	3	5-3Q(13)[3]	1.7412	36821	5
v=6											
6-4S(1)[3]	1.5015	31664	3	6-4Q(7)[3]	1.6829	34175	5	6-4O(4)[3,21]	1.7965	31306	8
6-4Q(3)[3]	1.6162	31664	5	6-4Q(9)[3,20]	1.7369	35992	6				
v=7											
7-5Q(5)[3]	1.7784	36591	3								

Notes: [a]maximum signal-to-noise ratio in the line image. In case of blends the reported number refers to the sum of the blended lines (unless the emission comes from different zones of the bow).

[1] blends with [Fe II] a^{2}H$_{11/2}$-a^{2}G$_{9/2}$
[2] contaminated by atmospheric absorption
[3] detected in the whole bow
[4] blends with 4-2S(4)
[5] blends with 3-1Q(2)
[6] blends with HI 4-9
[7] blends with 3-1O(9)

[8] blends with 6-4Q(9), HI4-10
[9] blends with 6-4O(4)
[10] blends with 4-2S(3)
[11] blends with 2-1S(9)
[12] blends with 2-0Q(9)
[13] blends with 4-2S(0)
[14] blends with [Fe II] a^{4}D$_{7/2}$−a^{4}F$_{9/2}$

[15] blends with 3-1Q(5)
[16] blends with 3-1S(0)
[17] blends with 2-0Q(2)
[18] blends with 5-3Q(7)
[19] blends with 4-2O(4)
[20] blends with 2-1S(15), HI 4-10
[21] blends with 2-1S(19)

observed line ratios, irrespective of the extinction values; *(ii)* the best 'recipe' to derive a reliable extinction estimate from [Fe II] lines is (at least when only the three considered lines are detected) to use the NS coefficients for the 1.321μm/1.644μm ratio and the Q-HFR coefficients for the 1.257μm/1.644μm ratio, that are 8% and 5% lower than our determinations; *(iii)* dedicated observations of objects with well known visual extinction should be performed to derive the [Fe II] Einstein A coefficients with sufficient accuracy.

3.1.2. Extinction map

Given the problems with the A coefficients outlined in the previous section, we have applied the following procedure to construct an extinction map across the HH99B bow from the observed [Fe II] lines: to minimise the effect of the uncertainties we used a number of line ratios involving bright lines from four energy levels (i.e. a^{4}D$_{7/2}$, a^{4}D$_{5/2}$, a^{4}D$_{3/2}$, a^{4}P$_{5/2}$) and distant in wavelength. With this set of ratios, and adopting, as a first attempt the NS coefficients, we determined the extinction in a very small region at the bow-head, where all the lines are detected with S/N ratio

larger than 30. This value has then been used to calibrate the extinction map obtained from the 1.25μm/1.644μm ratio, which is the only one detected well above the noise level (at least at 5σ) also in the bow flanks. Contours of the final map are shown in Figure 6: in a total area of $\sim$ 10 arcsec^2 variations of A$_V$ up to 4 mag are recognised. The highest A$_V$ values (4-5 mag) are found at the bow-head: if we correct the observed [Fe II] lines for them, the emission peak (see Figure 7) moves of about 0.6 arcsec towards north-east. Along the flanks A$_V$ is generally lower (up to 2-3 mag). Thus, the progressive fading in these zones of the Fe II emission can not be ascribed to an increasing extinction, but rather reflects low excitation conditions and/or low abundance of the gas-phase iron.

As described above, the main uncertainty on the extinction map arises from the adopted set of the A values. We have thus re-derived the same map from the 1.257μm/1.644μm ratio, now adopting our Einstein coefficients ratio of 1.24. We find that the largest difference between the two maps occurs at the emission peak, where it is of $\sim$ 0.6 mag. This implies a marginal increase in intrinsic line intensities (for example I(1.644μm) increases by 10%) and does not crit-

Table 2. Ionic lines observed in HH99B.

Line id.	λ_{vac} (μm)	E_{up} (K)	S/N$_{max}$[a]	Line id.	λ_{vac} (μm)	E_{up} (K)	S/N$_{max}$
				Ionic lines			
				[FeII] lines[b]			
a^{4}D$_{7/2}$–a^{6}D$_{9/2}$	1.2570	11446	700	**a^{4}D$_{1/2}$**–a^{6}D$_{3/2}$	1.2525	12729	20
a^{4}D$_{7/2}$–a^{6}D$_{7/2}$	1.3209	11446	130	a^{4}D$_{1/2}$–a^{6}D$_{1/2}$	1.2707	12729	24
a^{4}D$_{7/2}$–a^{4}F$_{5/2}$	1.9541	11446	7	a^{4}D$_{1/2}$–a^{4}F$_{5/2}$	1.6642	12729	18
a^{4}D$_{7/2}$–a^{4}F$_{9/2}$ [1]	1.6440	11446	720	a^{4}D$_{1/2}$–a^{4}F$_{3/2}$	1.7454	12729	21
a^{4}D$_{7/2}$–a^{4}F$_{7/2}$	1.8099	11446	99	**a^{4}P$_{5/2}$**–a^{4}D$_{5/2}$	1.9675	19387	20
a^{4}D$_{5/2}$–a^{6}D$_{9/2}$	1.1916	12074	7	a^{4}P$_{5/2}$–a^{4}D$_{1/2}$ [2]	2.1609	19387	5
a^{4}D$_{5/2}$–a^{6}D$_{7/2}$	1.2489	12074	17	**a^{4}P$_{3/2}$**–a^{4}D$_{7/2}$	1.7489	19673	9
a^{4}D$_{5/2}$–a^{6}D$_{5/2}$	1.2946	12074	70	**a^{4}P$_{1/2}$**–a^{4}D$_{5/2}$	1.8139	20006	62
a^{4}D$_{5/2}$–a^{6}D$_{3/2}$	1.3281	12074	42	**a^{2}G$_{9/2}$**–a^{4}D$_{7/2}$ [3]	1.2675	22797	7
a^{4}D$_{5/2}$–a^{4}F$_{9/2}$	1.5339	12074	30	**a^{2}G$_{7/2}$**–a^{4}D$_{7/2}$ [3]	1.1885	23552	16
a^{4}D$_{5/2}$–a^{4}F$_{7/2}$	1.6773	12074	157	**a^{2}P$_{3/2}$**–a^{4}P$_{5/2}$	2.0466	26417	4
a^{4}D$_{5/2}$–a^{4}F$_{5/2}$	1.8005	12074	35	a^{2}P$_{3/2}$–a^{4}P$_{3/2}$	2.1334	26417	5
a^{4}D$_{3/2}$–a^{6}D$_{3/2}$	1.2791	12489	41	a^{2}P$_{3/2}$–a^{4}P$_{1/2}$	2.2442	26417	4
a^{4}D$_{3/2}$–a^{6}D$_{1/2}$	1.2981	12489	23	**a^{2}H$_{11/2}$**–a^{2}G$_{9/2}$ [4]	2.2244	29265	21
a^{4}D$_{3/2}$–a^{4}F$_{7/2}$	1.5999	12489	46	**a^{2}H$_{9/2}$**–a^{2}G$_{9/2}$	2.0157	29934	10
a^{4}D$_{3/2}$–a^{4}F$_{5/2}$	1.7116	12489	13	a^{2}H$_{9/2}$–a^{2}G$_{7/2}$	2.2541	29934	5
a^{4}D$_{3/2}$–a^{4}F$_{3/2}$	1.7976	12489	36	**b^{4}P$_{1/2}$**–a^{4}P$_{3/2}$	1.1446	32242	4
				H lines			
3-5 (Paβ)	1.2822	151492	21	4-11	1.6811	156499	6
4-14	1.5884	156999	3	4-10[5]	1.7367	156226	6
4-13	1.6114	156870	4	4-9[6]	1.8179	155855	6
4-12	1.6412	156708	6	4-7 (Brγ)	2.1661	154583	12
				Other lines			
He I $^1P_1 - {}^1S_0$	2.0587	246226	3	[Ti II]a$^2F_{5/2}$-a$^4F_{3/2}$ [10]	2.1605	6652	5
He I $^3D - {}^3P$ [7]	2.0607	282101	8	[Ti II]a$^2F_{7/2}$-a$^4F_{9/2}$	2.2201	7040	5
He I $^3P_0 - {}^3D$ [7]	1.9522	289992	5	[Ti II]a$^2D_{5/2}$-a$^4F_{5/2}$	1.1560	12570	3
[P II]$^2D_2$-$^3P_1$	1.1471	12764	5	[Ti II]a$^4P_{3/2}$-b$^4F_{7/2}$	1.2036	13506	3
[P II]$^2D_2$-$^3P_2$ [8]	1.1886	12764	16	[Ti II]a$^2P_{3/2}$-b$^4F_{3/2}$	1.1028	14340	3
[Co II]b^3F_4-a$^5F_5$ [9]	1.5474	14119	5	[Ti II]a$^2H_{11/2}$-a$^2F_{/2}$	1.2695	17729	5

Notes: [a] maximum signal-to-noise ratio in the line image. In case of blends the reported number refers to the sum of the blended lines (unless the emission comes from different zones of the bow). [b] Lines coming from the same upper level are grouped, and the first term of each group is evidenced with bold-face characters.

[1] blends with 3-1O(7)
[2] blends with [Ti II]a$^2F_{5/2}$-a$^4F_{3/2}$ (fundamental transition)
[3] blends with [P II]$^1D_2$-$^3P_2$
[4] blends with 1-0S(0)
[5] blends with 2-1S(15), 6-4Q(9)

[6] blends with 2-1S(8)
[7] multiplet
[8] blends with [Fe II] a$^2G_{7/2}$-a^{4}D$_{7/2}$
[9] tentative identification
[10] blends with [Fe II] a^{4}P$_{5/2}$−a^{4}D$_{1/2}$

ically affects the derivation of the physical parameters of the atomic gas (see next section).

3.1.3. Electron density map and temperature

To derive the electron density along the bow structure, we selected seven intensity ratios (i.e. $I_{1.533}/I_{1.644}$, $I_{1.600}/I_{1.644}$, $I_{1.677}/I_{1.644}$, $I_{1.664}/I_{1.644}$, $I_{1.271}/I_{1.257}$, $I_{1.279}/I_{1.257}$, $I_{1.328}/I_{1.257}$), involving lines close in wavelength (their dfferential extinction is negligeable) and coming from levels with different critical densities (from $\sim 8\ 10^2$ to $3\ 10^5$ cm^{-3}) and similar excitation energy ($E_{up} \sim 11\,000$-$12\,000$ K), so that the dependence on the

temperature is very weak. All these line ratios have been simultaneously fitted with a NLTE code which solves the equations of the statistical equilibrium for the first 16 fine structure levels of [Fe II]. Spontaneuos rates are taken from NS, while energy levels and rates for electron collisions are adopted from Pradhan & Zhang (1993). Assuming $T_e = 10\,000$ K, we have constructed the electron density map shown in Figure 8; n$_e$ is of the order of 2-4 10^3 cm^{-3}, with a peak up to $6\,10^3$ cm^{-3} at the bow head[3]. These values are in the range commonly found in HH objects

[3] As we will see in the following, we estimate in this part of the bow T$_e\sim$ 16000 K. At this temperature the ratios involved in the electron density estimate can differ by less than 15% with
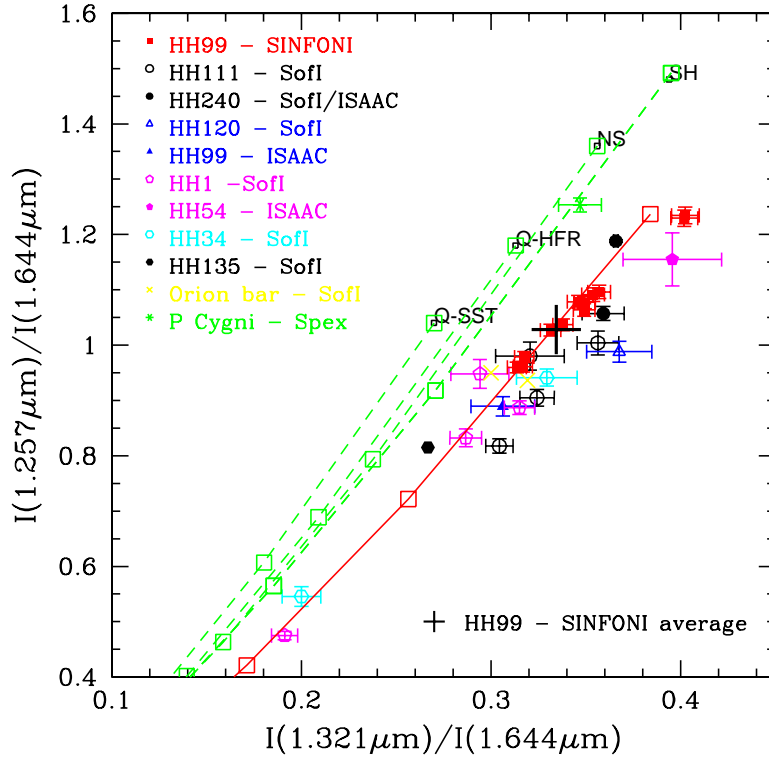
Fig. 5. $I(1.257\mu m)/I(1.644\mu m)$ vs. $I(1.321\mu m)/I(1.644\mu m)$ ratios measured in different objects (depicted with different symbols/colors). The HH99B-SINFONI data (red squares) have been computed in pixels where the S/N of each of the three lines is larger than 100, while other data are literature observations where S/N $\geq$ 30. Intrinsic line ratios predicted theoretically (Q-SST = Quinet et al. 1996 - SuperStructure; Q-HFR = Quinet et al., 1996 - Relativistic Hartree-Fock; NS = Nussbaumer & Storey, 1988), along with the observational point (SH) by Smith & Hartigan (2006), are labelled. Green dashed curves represent the extinction law by Rieke & Lebofsky (1985), starting from different theoretical points; open squares refer to $A_V = 0$, 5, 10 mag. The same extinction law (in red) has been applied to the $A_V = 0$ mag point derived from SINFONI data. This latter has been derived by applying to the average of the HH99B points (black cross) a visual extinction of 1.8 mag, as estimated from the $P\alpha/Br\gamma$ ratio (see text). References: HH99B - SINFONI: this work; HH111-, HH240-, HH120-SofI: Nisini et al., 2002; HH240- ISAAC: Calzoletti et al., 2008; HH99B - ISAAC : McCoey et al., 2004; HH1 - SofI: Nisini et al., 2005; HH54 - ISAAC: Giannini et al., 2007; HH34 - SofI: Podio et al., 2006; HH135 - SofI: Gredel, 2006; Orion bar - SofI: Walmsley et al., 2000; P Cygni - Spex: Smith & Hartigan, 2006.

from embedded jets (e.g. Nisini et al., 2005, Podio et al., 2006).

In a restricted area at the bow head of about 1 arcsec^2 (see Figure 1, middle right panel), we have detected 13 lines at high excitation (E_{up} between 20 000 and 30 000 K), which are suitable for evaluating the local electronic temperature. Of these, just four lines coming from the term a^{4}P (i.e. $1.749\mu m$, $1.814\mu m$, $1.967\mu m$, $2.161\mu m$) can be modelled, since for the remaining nine lines the collisional rates are unknown.

To that aim, we have enlarged our 16 level code by including further three fine structure levels for which the collisional coefficients are reported by Zhang & Pradhan (1995). Notably, the excitation energy of level #19 is around 32 000 K, well above than that of level #16 (less than 20 000 K): hence the temperature range that can be probed with the

19 level code is sensitively enlarged. Having fixed extinction and electron density from the maps of Figures 6 and 8, we fitted the de-reddened ratios with the $1.257\mu m$ line, integrated over the area where the a^{4}P lines are detected at S/N ≥ 5. Results are plotted in Figure 9, where the observed ratios are compared with the predictions of both the 16 and 19 level codes and for temperatures from 10 000 to 20 000 K. First, we note that while at $T_e \lesssim 10\,000$ K the inclusion of three further levels does not change the results of the 16 level code, strong differences emerge at higher temperatures (e.g. the ratio 1.257/1.749 decreases by about 70% at T_e=20 000 K). Second, ratios with the $1.814\mu m$, $1.967\mu m$, and $2.161\mu m$ lines well agree with $T_e \sim$ 16 000 - 17 000 K (the latter line has been de-blended from the fundamental line of [Ti II], using a NLTE model for this species, Garcia-Lopez et al., 2008).

Finally, we note that the ratio with the $1.749\mu m$ line implies $T_e \sim 8\,000$ K, that we consider not reliable because in

respect to those computed at T= 10000 K. This implies a very marginal increase of n$_e$.
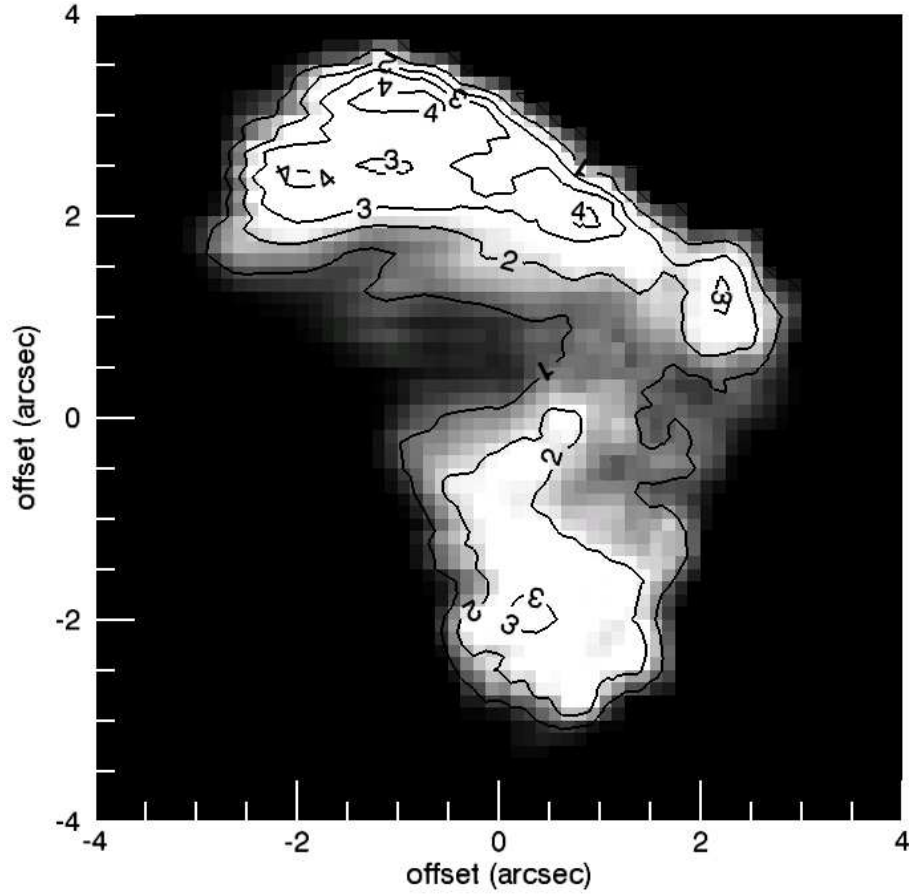
Fig. 6. Extinction map obtained from [Fe II] lines where contours from $A_V=1$ mag to $A_V=4$ mag are shown. The NS Einstein A coefficients have been adopted.
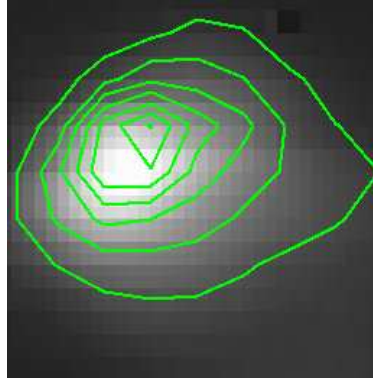

Fig. 7. . De-reddened contours of 1.257μm intensity, overlaied with the image acquired in the same line.

the same spatial region examined here also bright hydrogen and helium recombination lines are observed (see Figure 1). For this line, however, neither evident discrepancies in the different computations of the Einstein coefficients (all the available lists give similar values, see Sect.3.1.1), nor observational biases (e.g. extinction, blending with other lines) are able to explain the disagreement with the other ratios.

3.1.4. [Fe II] abundance

The gas-phase Fe abundance x(Fe) is a measure of the shock efficiency in disrupting the cores of the dust grains where iron is locked in quiescent conditions (e.g. May et al.,

2000). Estimates of x(Fe) in shock environments so far have given sparse results, from values close to solar abundance (e.g. Beck-Winchatz, Bohm & Noriega-Crespo, 1996), up to intermediate (Nisini et al., 2002) and very high depletion factors (Mouri & Taniguchi, 2000, Nisini et al., 2005). A powerful way to estimate the percentage of gas-phase iron (δ_{Fe}) based on [Fe II]/[P II] line ratios has been proposed by Oliva et al. (2001). Since phosphorus and iron have similar ionisation potentials and radiative recombination coefficients, they are expected to be in the first ionised state in comparable percentages; moreover, the near-IR lines of Fe II and P II have similar excitation energies and critical densities and therefore are excited in similar physical con-
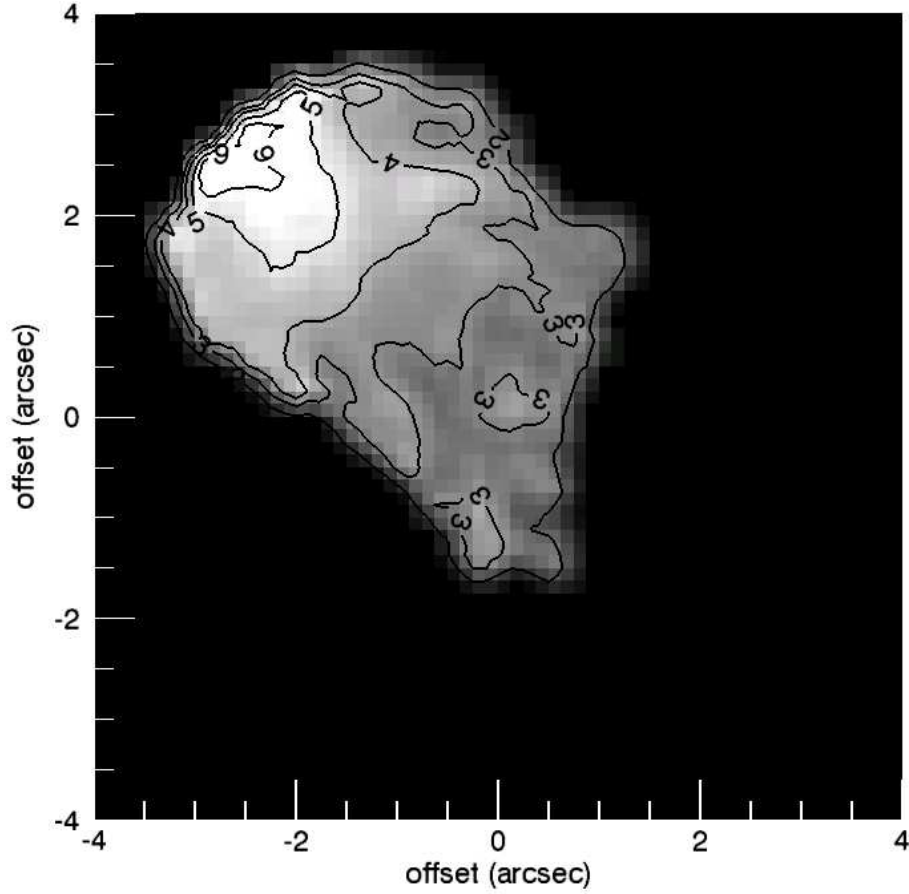
**Fig. 8.** Electron density map as derived from [Fe II] line ratios. Contours are in units of 10^3 cm^{-3}.
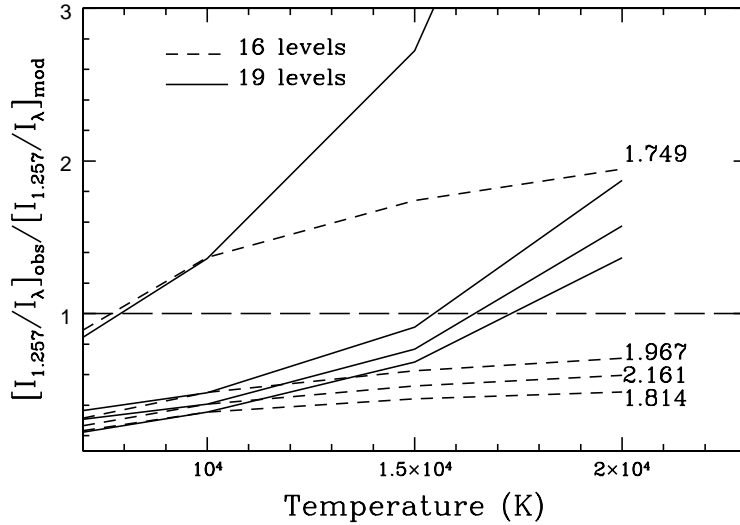
Fig. 9. $[I_{1.257}/I_\lambda]_{obs}/[I_{1.257}/I_\lambda]_{mod}$ plotted vs. the electronic temperature for four [Fe II] lines. The results for the Fe NLTE model at 16 and 19 levels are shown for comparison.

ditions. Hence, [Fe II]/[P II] line ratios are good indicators of the relative abundance of the two species, and more specifically, because phosphorus is a non-refractory species, of the degree of iron depletion. In HH99B two [P II] lines are de-tected, at 1.1471 and 1.1885 μm, this latter barely blended with a [Fe II] line (see Table 1). Oliva et al. derive:

$$\frac{x(\text{Fe})}{x(\text{P})} \simeq 2 \times \frac{I([\text{Fe II}]1.257)}{I([\text{P II}]1.188)} \simeq \frac{I([\text{Fe II}]1.257)}{I([\text{P II}]1.147)} \qquad (1)$$
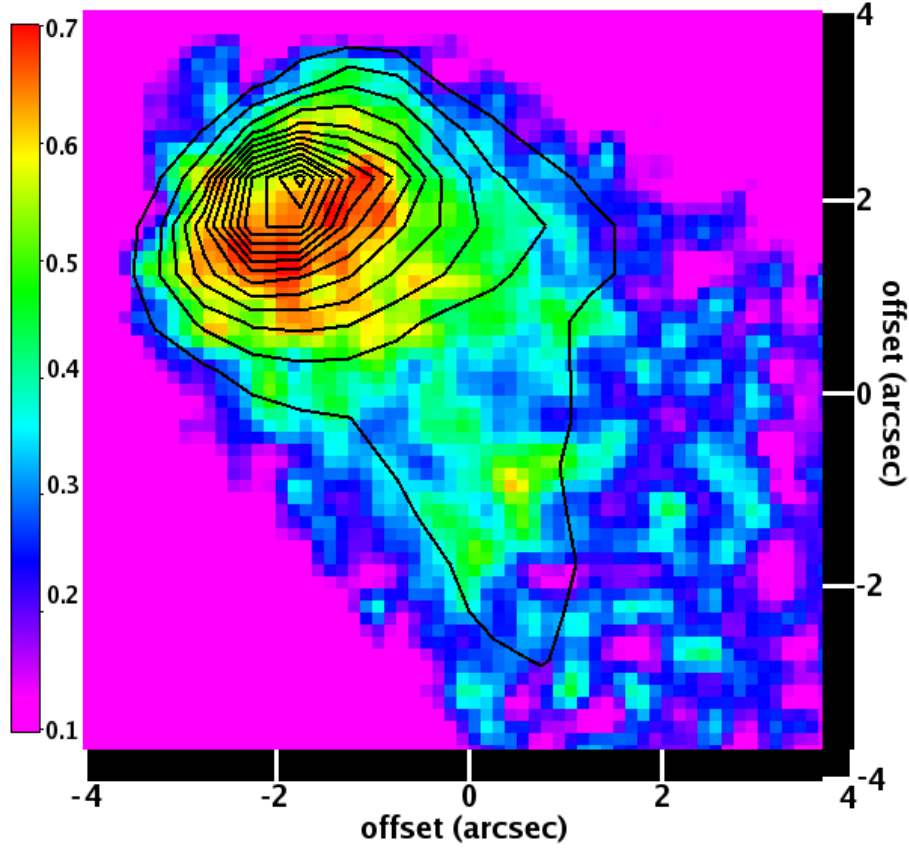
Fig. 10. Map of the percentage of iron in gas-phase with overlaied the intensity contours of the [Fe II] 1.257μm line.

This equation, as stated by the authors, is accurate to within a factor of 2 for all temperatures and densities expected within the shock. By assuming a solar Fe /P abundance ratio of ~ 120 (Asplund, Grevesse & Sauval, 2005) we have derived a map of the percentage of gas-phase iron (see Figure 10). A strong decrease in the percentage of gasphase iron occurs from the bow-head (70%) towards the zones behind (up to 20%), with an average uncertainty of about 15%, estimated from the propagation of the errors in both the two considered images. Notably, theoretical predictions for the degree of iron depletion as a function of the shock velocity (Jones, 2000) imply that this latter should exceed 100 km s^{-1} for $\delta_{Fe} \gtrsim 0.20$, a condition verified in our case even in the bow flanks.

3.2. H$_2$ analysis

3.2.1. Extinction map

Looking at the line images of Figure 1 it is evident that the bulk of the H$_2$ emission comes from the bow flanks. Since these parts of the bow are not covered in the extinction map obtained with [Fe II] lines (see Figure 6), this latter cannot be used to de-redden the H$_2$ emission. Hence, as a first step of the H$_2$ line analysis, we have derived a new extinction map. Out of a number of ratios of lines coming from the same upper level, we considered only the three ratios (1-0S(1)/1-0Q(3), 2-0S(1)/2-1S(1), 2-0Q(3)/2-1S(1)) of lines detected at S/N per pixel larger than 5 over the whole emission region. Since the one at the largest S/N (1-0S(1)/1-0Q(3)), suffers from the poor atmospheric transmission at 2.42μm of the 1-0Q(3), we have used the other two ratios

as calibrators and the 1-0S(1)/1-0Q(3) ratio to probe the differential extinction along the shocked region. The Rieke & Lebofsky (1985) extinction law was adopted. The final map is shown in Figure 11: the covered zone somewhat complements the A$_V$ map constructed from [Fe II] lines, with a partial spatial overlap in the areas corresponding to knots B3 and B1 of D99. The A$_V$ values typically range from 1 to 4 mag, in substantial agreement with those inferred from [Fe II] emission: therefore this result demonstrates that the reddening *within* the shock does not change significantly and that the A$_V$ variations mainly arise from the foreground material inside the cloud. Our result contrasts with the general trend observed both in other Herbig-Haro objects (e.g. Nisini et al., 2002, Giannini et al., 2004) and in HH99B itself (MC04), where the extinction computed from [Fe II] lines is systematically higher than that probed with H$_2$ lines. This may stem because in these cases the extinction was computed from the 1.257μm/1.644μm ratio, for which the A coefficients of NS have been adopted (see Sect.3.1.1).

3.2.2. Temperature map

The temperature of the molecular gas can be obtained from a Boltzmann diagram (e.g. Gredel, 1994), plotting $\ln(N_{v,J}/g_J)$ against $E_{v,J}/k$. Here $N_{v,J}$ (cm^{-2}) is the column density of the level (v, J), $E_{v,J}$ (K) its excitation energy and $g_J = (2J+1)(2I+1)$ the statistical weigth (here we assume that I=0,1 for para- and ortho-H$_2$). If the gas is thermalised at a single temperature, the data points align onto a straight line, whose slope gives the gas tempera-
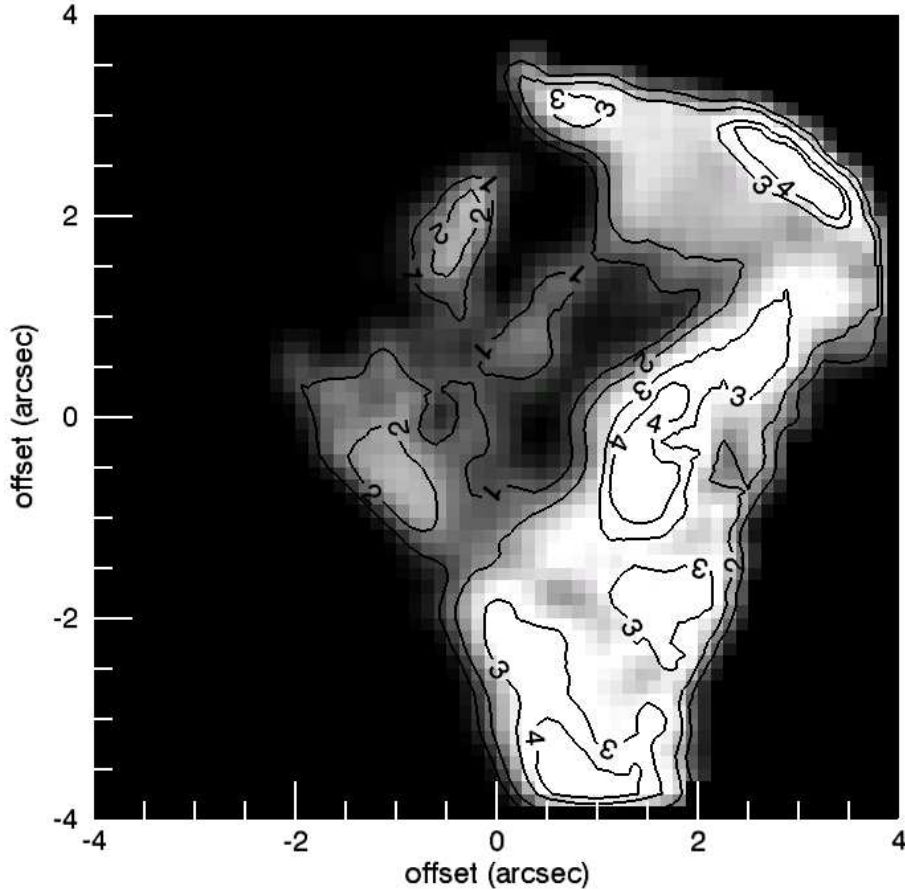
**Fig. 11.** Extinction map as derived from H$_2$ line ratios. Contours from A$_V$=1 to 4 mag are shown.

ture. In this diagram, points that refer to transitions from the same upper level do overlay each other, once corrected for extinction effects. We applied this method to all the pixels of the H$_2$ images, and the resulting map is shown in Figure 12, where contours of temperature are given in units of 10^3 K. Three results can be taken from this map: *(i)* a temperature gradient from $\simeq 2\,000$ K up to 6000 K occurs from the receding parts of the shock towards the head. We underline that this gradient can be traced because of the very large number of H$_2$ lines detected, which cover the Boltzmann diagram up to excitation energies of $\sim 38\,000$ K, therefore sensitively enlarging the dynamical range of temperatures typically probed with H$_2$ near-infrared lines; *(ii)* two different behaviours in the Boltzmann diagram occur between the bow-head and the flanks (see the insets in Figure 12): H$_2$ appears fully thermalised (at T~ 5000 K) at the bow-head (hence here the contours give directly the gas temperature), while a curvature exists among the points in the southern flank diagram, so that at least two temperature components can be traced. In these parts of the bow the contours indicate the *average* of these temperatures. The outlined behaviour can be generalised to the whole bow structure and likely reflects, from one side, that fluorescence can be discarded as a possible excitation mechanism, since it implies strong departures from thermalisation (Black & van Dishoeck, 1997), and, from the other side, that different shock mechanisms are at work. In fact, the response of the level populations to the shock parameters can be seen in the Boltzmann diagram. Roughly speaking, an enhancement of the shock velocity increases the rate of

collisions that vibrationally excite the H$_2$ molecules and favours thermodynamical equilibrium: thus the thermalisation observed along the head would testifies the presence of a fast shock. If this were the case, a C-type shock should be favoured, otherwise H$_2$ could not survive (at high temperatures) against dissociation (e.g. Le Bourlot et al., 2002, Flower et al., 2003). The alternative possibility that the observed H$_2$ emission arises from re-forming H$_2$ onto dust grains can be reasonably discarded. In fact, the timescale of this process is of the order of $10^{17}/n$ s^{-1} (Hollenbach & McKee, 1979), being n the density of the gas after the compression due to the shock passage. For reasonable values of this parameter (10^4-10^7 cm^{-3}), and assuming a velocity of the downstream gas of the order of 10 km s^{-1}, the distance covered by the gas at the bow-head should be between 10^{16} and 10^{19} cm, definitively longer than the linear dimension of knot B0, i.e. $\sim 5\ 10^{15}$ cm; *(iii)* from the same Boltmann diagrams a marked difference in the column density of the warm H$_2$ (from the intercept of the straight line) emerges. For example, from the insets of Figure 12 we derive N(H$_2$) = 2 10^{17} cm^{-2} and 3 10^{16} cm^{-2} at the flank and at the bow-head, respectively. If the same shock lengths are assumed for these regions, it derives that about 85% of the molecular gas must get destroyed in the most excited part of the shock (although H$_2$ emission is still observed).

3.3. H analysis

At the bow-head we observe hydrogen recombination lines of the Brackett series along with the Paβ line. The S/N
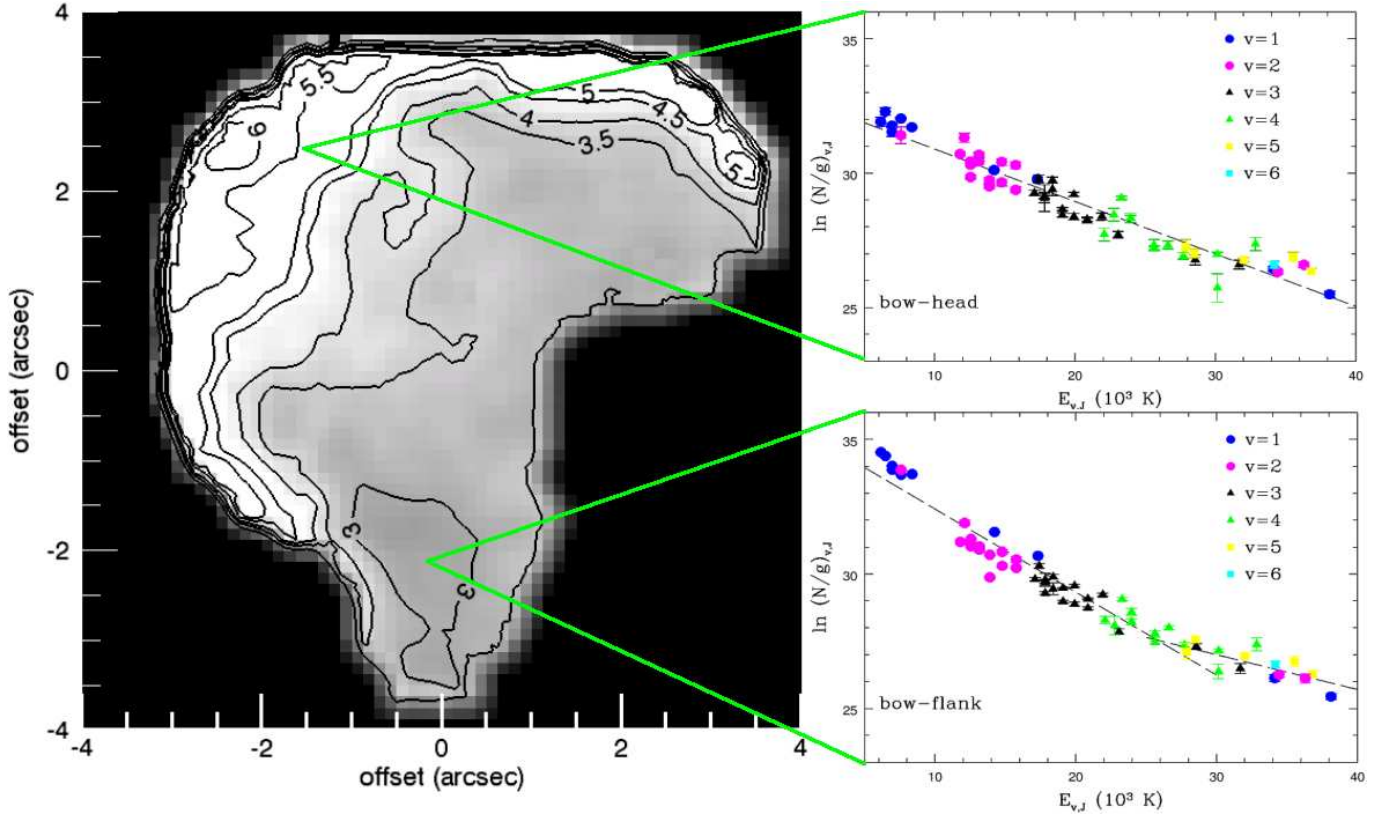
Fig. 12. Temperature map (in 10^3 K) as derived from H_2 line ratios. As an example, we show the rotational diagrams in two points of the bow: while at the bow-head H_2 appears thermalised at (T$\sim$ 5000 K), in the southern flank two temperature components co-exist, with an average temperature (corresponding to the point shown in the map) of $\sim$ 2800 K.

ratio of these lines, but Brγ and Paβ, is so low, however, that detailed modelling is prohibitive. Thus, we have used just the Paβ/Brγ ratio to derive an independent estimate of the extinction. Assuming case B recombination (Storey & Hummer, 1995), we obtain $A_V = 1.8\pm1.9$ mag.
More interesting parameters, i.e. the hydrogen fractional ionisation, x_e, and the hydrogen post-shock density, $n_H = n_e/x_e$, are obtainable from the observed intensity ratio [Fe II]1.257/Paβ. As described in detail in Nisini et al.(2002), under the assumption that iron is singly ionised, such a ratio can be expressed as:

$$x_e = \delta_{Fe}(\text{Fe}/\text{H})_\odot \left(\frac{[\text{Fe II}]1.257}{Pa\beta}\right)^{-1} \frac{\epsilon_{[\text{Fe II}]1.257}}{\epsilon_{Pa\beta}} \quad (2)$$

with δ_{Fe} the gas-phase iron fraction with respect to the solar Fe abundance, (Fe/H)$_\odot$ and $\epsilon_{[\text{Fe II}]1.257}$ and $\epsilon_{Pa\beta}$ (in erg cm^3 s^{-1}) the emissivities of the two lines, taking $\epsilon_{Pa\beta}$ from Storey & Hummer (1995). The above quantity was computed for the physical conditions derived at the bow-head, i.e. T=16 000 K, n_e=6 10^3 cm^{-3}, $\delta_{Fe} \sim 0.7$ and having taken (Fe/H)$_\odot$ = 2.8 10^{-5} (Asplund, Grevesse & Sauval 2005). This leads to $x_e \sim$ 0.4-0.5 and n_H between 0.8 and 1.4 10^4 cm^{-3}. In the receding parts of the shocks, the fractional ionisation cannot be directly computed, since we have no estimates for the electron temperature. However, under the reasonable assumption that T$_e \lesssim$ 10 000 K a sharp decrease of x_e is expected: for example, for the regions where δ_{Fe}=0.3-0.4, we find $x_e \sim$ 0.2-0.3. These estimates are in agreement with those inferred along other

Herbig-Haro objects through optical line diagnostics (e.g. Bacciotti & Eislöffel, 1996, Hartigan & Morse, 2007) and with those inferred in a number of jets by combining optical and infrared observations (Nisini et al., 2005, Podio et al., 2006).

4. Kinematical properties

4.1. H_2

In this section we intend to characterise the kinematical parameters of the shock(s) in HH99B. This topic was already discussed by D99, and we compare here our results with those found in that work. The higher spectral resolution (R$\sim$ 15 kms^{-1}) of D99, obtained with echelle spectroscopy, has revealed that the peak velocity of the H_2 2.122μm line moves progressively from slightly blue-shifted values near the shock front towards red-shifted values in the flanks, and has been interpreted in the framework of a receding bow-shock oriented with respect to the line of sight of about 45°.

Nominally, the spectral resolution of our K band observations would not permit us to reveal variations of the order of those measured by D99. This limitation, however, is partially compensated by the very high S/N ratio at which we detect the 2.122μm line. A trend on both the peak velocity and on the profile shape can be followed along the bow structure, although we cannot give precise numerical estimates on the line parameters (v$_{peak}$, FWHM). Our results are presented in Figure 13, where the contours of the
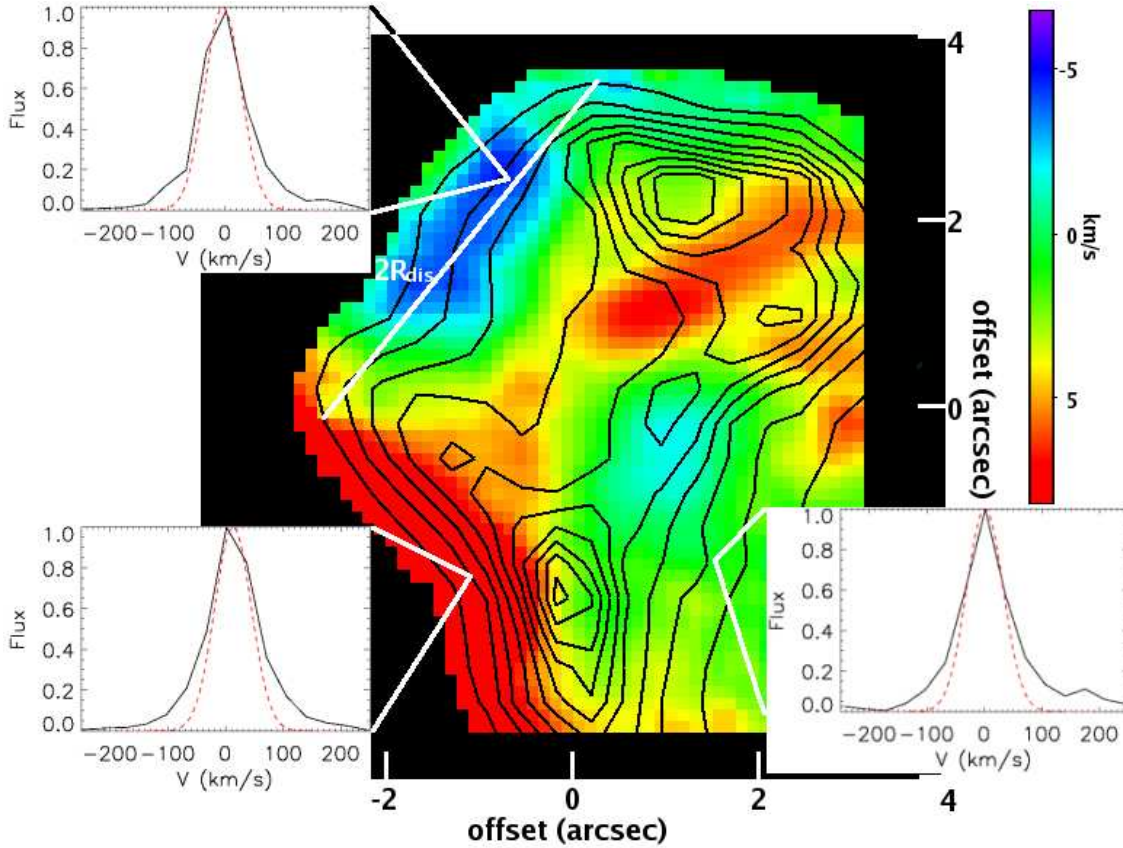
Fig. 13. Local standard of rest (LSR) velocity map of the 2.122μm line peak, with superimposed line intensity contours. We indicate with a white line the diameter $2R_{dis}$ of the last cap beyond which the bulk of H_2 is dissociated (see Sect.4.2). Insets show the line profile observed at the bow head (top left), in the southern flank (bottom left) and at the bow centre (bottom right). Blue and red asymmetries are visible at the bow head and along the flanks, while the line is symmetric toward the centre. The instrumental profile, measured on OH atmospheric lines, is shown for comparison (red dashed line).

2.122μm line intensity (de-reddened) have been superposed on the v_{peak} map.

Overall, our results confirm those of D99: the line profile presents a blue-shifted component towards the shock front at the bow head (B0). The opposite occurs along the two flanks and especially along the edge of the B1 flank (not covered by the echelle spectra in D99), where the line peak is shifted of $\sim +15$ km s^{-1} with respect to the line profile at the head. Analogous to the spectra of D99, the 2.122μm profile does not show double peaked components, as generally expected for a parabolic bow structure (Schultz, Burton & Brand, 2005) though it does become wider near the centre of the bow, where the opposite sides are seen in projection. Here the observed FHWM$_{obs}$ is 85-105 km s^{-1}, that, deconvolved with the instrumental profile, measured on atmospheric OH lines, roughly gives an intrinsic line width of $\sim$ 20-40 km s^{-1}. The agreement with previous observations is also mantained along the bow flanks, where the profile width becomes narrower decreasing toward the spectral resolution limit on the intrisic width of $\sim$ 20 km s^{-1}. As for the line peak, a sudden increase of FHWM$_{obs}$ is registered at the edge of the southern flank, where we measure up to $\sim$ 115 km s^{-1}, i.e. an intrinsic width of $\sim$ 70 km s^{-1}. This is close to the maximum shock velocity ($\sim$ 80 km s^{-1}) at which H_2 can survive against dissociation, predicted by the C-shock model by Le Bourlot et

al. (2002). This last topic will be further discussed in the next section.

4.2. [Fe II]

We have performed the kinematical analysis of the ionic gas component on the two brightest [Fe II] lines at 1.257 and 1.644μm. Both appear resolved in velocity and give similar results for the line profile shape (which is Gaussian across the whole bow), the intrinsic line width, the peak position and the FWZI. This last result gives a direct measure of the shock speed at the bow apex (Hartigan, Raymond & Hartmann, 1987): we obtain $v_{bow} = 115\pm5$ km s^{-1}, which agrees well with the prediction by D99 (80-120 km s^{-1}) derived from the overall shape of the bow and the characteristics of the H_2 2.122μm line profile.
In Figure 14 we show the radial velocity map of the 1.644μm line: this appears red-shifted over the whole bow structure, the maximum shift occurring towards the image centre. We intepret this behaviour as a geometrical effect due to the inclination of the bow with respect to the line of sight. Indeed, if the bow is observed at a certain angle $\alpha \neq 0°$, $180°$, the peak of the radial velocity component is seen offset from the bow apex. Following the procedure described in Appendix A, we are able to express the projected distance (D') between the emission and the radial velocity peaks as a func-
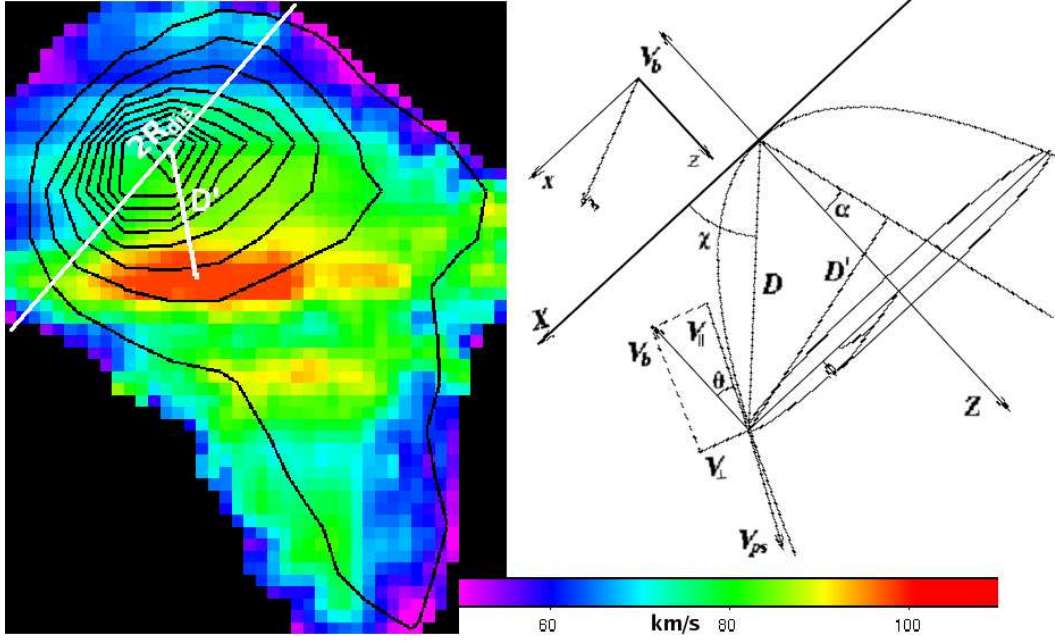
Fig. 14. *Left panel*: local standard of rest (LSR) velocity map of the 1.644μm line peak, with superimposed line intensity contours. The line is red-shifted along the bow-structure, with a peak at about $+70$ km s^{-1}. The projection D' along the line of sight of the distance between the line emission peak and the maximum radial velocity is shown, together with the diameter $2R_{dis}$ (see caption of Figure 13). *Right panel*: schematic view of the parabolic geometry assumed for the bow-shock. The apex coincides with the origin of the coordinate system. $R=\sqrt{x^2+y^2}$, is the radius at the distance z along the bow axis, ϕ is the azimuthal angle around the z-axis, θ is the angle between the bow direction and the tangent to the parabolic surface (at each θ the shock velocity at the apex, v_b, is de-composed in $v_{\parallel}$ and $v_{\perp}$) and α is the angle, lying on the x-z plane, between the z-axis and the line of sight. D is the distance between the line emission peak and the maximum radial velocity and D' its projection onto the sky plane.

tion of α and the H$_2$ breakdown velocity (v_{dis}), once the relationship between this latter and the parameter b regulating the bow (parabolic) shape is defined. The result is depicted in Figure 15: interestingly, we found α values close to that inferred by D99 for a range of v_{dis} between 70 and 90 km s^{-1}. These values can be considered as an indirect measurement of a parameter whose theoretical predictions have been widely discussed over the last decades: a first value of 24 km s^{-1} was inferred by Kwan (1977), subsequently Draine, Roberge & Dalgarno (1983) found v_{dis}=50 km s^{-1}, a result confirmed by Smith & Brand (1990) and Smith (1991). More recently, Le Bourlot et al. (2002) have shown that v_{dis} can increase up to 80 km s^{-1} for values of the pre-shock density around 10^3 cm^{-3}. Our measurement is therefore in agreement with this latter prediction. Moreover, $v_{dis} \sim 80$ km s^{-1} is consistent with the FWHM of the 2.122μm line profile measured in the southern flank (Sect. 4.1), and reinforces the hypothesis that a fast, continuous shock is responsible for the excitation of the molecular gas at the apex of the bow (Sect.3.2.2).

5. Concluding remarks

We have presented bi-dimensional, deep near-infrared spectral images of the bow shock HH99B. These have allowed us, for the first time, to accurately derive the physical parameters of both the molecular and ionic gas components (summarised in Table 3, where our results are compared with those derived in previous works), and, at the same time, to characterise the geometry and the kinematical

properties of the flow. The main results of this study are the following:

- More than 170 emission lines have been detected, mainly ro-vibrational H$_2$ and [Fe II] lines, many of them never observed before in an Herbig-Haro object. In addition, transitions of hydrogen and helium recombination and fine structure lines of [P II], [Ti II], and possibly [Co II] have been observed.
- A clear bow-shape morphology emerges from the line intensity maps. As shown in Figures 2-4, [Fe II] and other ionic emission peaks definitely at the bow-head (B0), being strong also in the knot B2 immediately behind. In contrast, H$_2$ emission delineates the bow flanks, peaking in the knots B1 and B3. Notably, the H$_2$ lines with the highest excitation energy ($E_{up} \gtrsim 30\,000$ K) show a different morphology, being strong towards the bow-head. This implies that H$_2$ still survives in this zone, in spite of the significant temperature enhancement there.
- Extinction maps have been derived from the analysis of both [Fe II] and H$_2$ lines. These give similar results, with A$_V$ ranging between 1 and 4 mag.
- A detailed electron density map has been obtained in the framework of NLTE approximation for [Fe II] line emission. This remains almost constant in the [Fe II] emission zone, peaking towards the bow-head. From the same emission, we are able to probe a variation of the electron temperature, which falls from $\sim 16\,000$ K at the apex to less than $10\,000$ K in the receding parts of the bow.
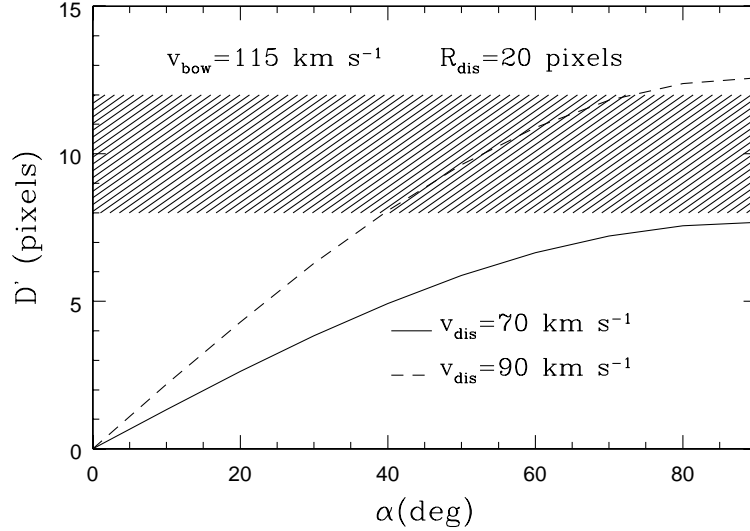
Fig. 15. Projection over the sky plane of the distance between the [Fe II]1.644μm emission peak and the maximum radial velocity, plotted against the bow inclination angle α. The hatched area defines the uncertainty on D', estimated as the maximum and minimum distance between the 1.644μm line peak and the points where the maximum shift in velocity is registered (those coloured in red in Figure 14, left panel). The curves refer to different assumptions for the H$_2$ breakdown speed, v$_{dis}$, having measured the shock velocity at the bow apex, v$_{bow}$ and the radius R$_{dis}$ (see Appendix A). The observations are matched for v$_{dis}$ between 70 and 90 km s^{-1}.

Table 3. Physical parameters estimated in HH99B.

Parameter	This work	MC04	D99
A$_V$(Fe II) (mag)	1-4	4-10	-
A$_V$(H$_2$) (mag)	2-4	<4	<4.6
A$_V$(H) (mag)	~2	-	-
n$_e$ (cm^{-3})	3-6 10^3	-	-
T$_e$ (K)	$\leq$ 17 000	-	-
T$_{H_2}$ (K)	2 500 - 6 000	2 000 - 4 000	-
N$_{H_2}$ (cm^{-2})	3 10^{16} - 2 10^{17}	-	-
$\delta_{\text{Fe II}}$	0.2-0.7	0.25	-
x$_e$	0.2-0.5	-	-
n$_H$ (cm^{-3})	~10^4 (post-shock)	10^4 (pre-shock)	-
v$_{bow}$ (km s^{-1})	110-120 ([Fe II])	50 ([Fe II])	80-120 (H$_2$)
inclination angle ($^\circ$)	40-60	-	45

- An iron depletion degree not higher than 30% has been inferred at the bow apex, which testifies in favour of a J-type shock as the main excitation mechanism in this part of the bow. In this same zone, we infer a fractional ionisation of $\sim$ 0.6 and a post-shock density of $\sim$ 10^4 cm^{-3}.
- Analysis of H$_2$ line emission has allowed us to probe the molecular temperature variation. We find that at the bow apex thermalisation has been reached at T$\sim$ 6 000 K, likely due to the presence of a fast, non-dissociative shock. On the contrary, along the flanks different temperature components are simultaneously present. A decrease of about a factor of ten is registered in the H$_2$ column density going from knots B1/B3 toward knot B0. Both these circumstances are not accounted for by models which have attempted to interpret the H$_2$ emission on HH99B on the basis of fewer lines. Therefore,

the conclusions of such models should be tested in the light of this new piece of information.
- From the brigthest [Fe II] and H$_2$ lines we have been able to probe the kinematical properties (e.g. shock velocity) of the shocked gas. In particular, we confirm the result by D99 according to which HH99 is a red-shifted, receding bow.
- The radial velocity map of [Fe II] emission has been interpreted in the framework of the bow geometry. From this map we have consistently inferred the bow inclination angle and defined a range of 70-90 km s^{-1} for the H$_2$ breakdown velocity. These values are in agreement with the prediction of Le Bourlot et al.(2002) of v$_{dis}$ up to 80 km s^{-1}. We propose our method as a valuable tool to derive the jet inclination angle (if larger than 10-20°) in cases where proper motion is unknown.
- The kinematical parameters of the [Fe II] emission estimated in this work do not confirm the model predictions

by MC04. In particular, the argument that the [Fe II] lines originate in a pure J-type shock with $v_{shock} \sim 50$ km s^{-1} contrasts with our measure of $v_{shock} \sim 110\text{-}120$ km s^{-1}. Thus, the modelling of the [Fe II] emission may have to be revised.

6. Acknowledgments

References

Asplund, M., Grevesse, N., & Sauval, A.J. 2005, Cosmic Abundances as Records of Stellar Evolution and Nucleosynthesis, 336, 25
Bacciotti, F., & Eislöffel, J. 1999, A&A, 342, 717
Black, J.H., & van Dishoeck, E.F. 1997, ApJ, 322, 412
Beck-Winchatz, B., Bohm, K-H, & Noriega-Crespo, A. 1996, AJ, 111, 346
Bonnet, H., Abuter, R., Baker, A., et al. 2004, The ESO Messenger 117, 17
Caratti o Garatti, A., Eislöffel, J., Froebrich, D., et al. 2007, A&A, submitted
Cardelli, J. A., Clayton, G. C.& Mathis, J. S. 1988, ApJ, 329,33
Calzoletti, L., Giannini, T., Nisini B., et al., 2008, in preparation
Draine, B.T. 1980, ApJ, 241, 1021
Draine, B.T., Roberge, W.G., & Dalgarno, A. 1983, ApJ, 264, 485
Davis, C.J., Smith, M.D., Eislöffel, J., Davies, J.K. 1999, MNRAS, 308, 539 (D99)
Eisenhauer, F., Abuter, R., Bickert, K. et al., 2003, SPIE 4841, 1548
Eislöffel, J., Smith, M.D., & Davis, C.J. 2000, A&A, 359, 1147
Flower, D.R., Le Bourlot, J., Pineau des Forets, G. Cabrit, S. 2003, MNRAS, 341, 70
Garcia-Lopez, R., Nisini, B., Giannini, T., et al. 2008, A&A, submitted
Giannini, T., McCoey, C., Caratti o Garatti, A., Lorenzetti, D., Flower, D. 2004, A&A, 419, 999
Giannini, T., McCoey, C., Nisini, B., et al. 2007, A&A, 459, 821
Gredel, G. 1994, A&A, 292, 580
Gredel, G., 2006 A&A, 457, 157
Jones, A.P. 2000, JGR, 105, 10257
Hartigan, P. 1989, ApJ, 339, 987
Hartigan, P., & Graham, J.A. 1987, AJ, 93, 913
Hartigan, P., & Morse, J. 2007, ApJ, 660, 426
Hartigan, P., Raymond J., & Hartmann L. 1987, ApJ, 316, 323
Hollenbach, D., & McKee, C. 1979, ApJ, 41, 555
Hollenbach, D., & McKee, C. 1989, ApJ, 342, 306
Kwan, J. 1977, ApJ, 216, 713
Lesaffre, P., Chieze, J.-P., Cabrit, S., Pineau des Forets, G. 2004, A&A, 427,147(a)
Lesaffre, P., Chieze, J.-P., Cabrit, S., Pineau des Forets, G. 2004, A&A, 427,157(b)
Le Bourlot, J. Pineau des Forets, G. Flower, D.R., Cabrit, S. 2002, A&A, 390, 369
Lidman, C., & Cuby, J.G. 2000, ATLAS of OH lines
Marraco, H.G., & Rydgren A.E. 1981, AJ, 86, 62
Mouri, H., & Taniguchi, Y. 2000, ApJ, 534, L63
May, P.W., Pineau des Forets,G., Flower, D.R., et al. 2000, MNRAS, 318, 809
McCoey, C., Giannini, T., Flower, D.R., Caratti o Garatti, A. 2004, MNRAS, 353, 813 (MC04)
Modigliani, A., Ballester, P. & Peron, M. 2007, SINFONI Pipeline User Manual, http://www.eso.org/projects/dfs/dfs-shared/web/vlt/vlt-instrument-pipelines.html
Nisini, B., Bacciotti, F., Giannini, T., et al. 2005 A&A, 441, 159

Nisini, B., Caratti o Garatti, A., Giannini, T., Lorenzetti, D. 2002, A&A, 393, 637
Nussbaumer, H., & Storey, P.J. 1988, A&A, 193, 327
O'Connell,B., Smith, M.D., & Davis, C.J. 2004, A&A, 419, 475
Oliva, E., Marconi, A., Maiolino, R., et al. 2001 A&A, 369, 5
Pradhan, A.K., & Zhang, H.L. 1993, ApJ, 409, L77
Podio, L., Bacciotti, F., Nisini, B., et al. 2006, A&A, 456, 189
Reipurth, B., & Bally, J. 2001, ARAA, 39, 40
Rieke, G.H., & Lebofsky, M.J. 1985, ApJ, 288, 618
Quinet, P., Le Dourneuf, M., & Zeippen, C.J. 1996, A&AS, 120, 361
Schultz, A.S.B., Burton, M.G., & Brand, P.W.J.L. 2005, MNRAS, 358, 1195
Smith, M.D. 1991, MNRAS, 252, 378
Smith, M.D., & Brand, P.W.J.L. 1990, MNRAS, 248, 108
Smith, M.D., Froebrich, D., & Eislöffel, J. 2003, ApJ, 592, 245
Smith, M.D., & Mac Low, M.-M. 1997, A&A, 326, 801
Smith, M.D., & Rosen, A. 2003, MNRAS, 339,133
Smith, N., & Hartigan, P. 2006, ApJ, 638, 1045
Storey, P.J., & Hummer, D.G. 1995, MNRAS, 272, 41
Walmsley, C. M., Natta, A., Oliva, E., Testi, L. 2000, A&A, 364, 301
Wilking, B.A., McCaughrean, M. J., Burton, M.G. et al., 1997, AJ, 114, 2029
Zhang, H. L., & Pradhan, A. K. 1995, A&A, 293, 953

Appendix A: Derivation of inclination angle and H$_2$ breakdown velocity

With reference to Figure 14, right panel, we assume that the bow has a parabolic geometry ($z = R^2/2b$), where the apex coincides with the origin of the coordinate system. R$=\sqrt{x^2 + y^2}$, is the radius at the distance z along the bow axis, ϕ is the azimuthal angle around the z-axis, θ is the angle between the bow direction and the tangent to the parabolic surface and α is the angle, lying on the x-z plane, between the z-axis and the line of sight. This latter can be inferred by measuring in the radial velocity map (Figure 14, left panel) the projection D' over the sky plane of the distance between the line emission peak and the maximum radial velocity (D$' =10\pm2$ pixels). We have:

$$D' = D \cos(\chi - \alpha) = \sqrt{z_{max}^2 + 2z_{max}b} \times \cos(\chi - \alpha) \quad (A.1)$$

where z$_{max}$ is the distance along the z-axis at which the radial velocity reaches its maximum. We firstly estimated the b parameter. Since the molecular hydrogen does not emit over the entire bow surface, there is a leading edge which divides the bow into two different zones: a dissociation cap, beyond which the emission comes from atomic/ionic elements and a molecular hydrogen emitting flank. Therefore, it is possible to define as z$_{dis}$ the position along the z-axis where the leading edge plane is located: certainly it depends on the shock velocity at the bow apex, v$_{bow}$, on the H$_2$ breakdown velocity, v$_{dis}$ and on the shape of the bow surface. Setting v$_{dis}$ = v$_{bow}$ sinθ_{dis} and, since for a generic angle θ, tanθ=dR/dz:

$$v_{dis} = v_{bow} \left. \frac{dR/dz}{\sqrt{1 + \left(\frac{dR}{dz}\right)^2}} \right|_{z=z_{dis}} \quad (A.2)$$

Substituting the parabolic equation in this formula, we get:

$$z_{dis} \frac{b}{2} \left[\left(\frac{v_{bow}}{v_{dis}} \right)^2 - 1 \right] \quad (A.3)$$

and

$$b = \frac{R_{dis}^2}{2z_{dis}} = \frac{R_{dis}}{\sqrt{\left(\frac{v_{bow}}{v_{dis}}\right)^2 - 1}} \qquad (A.4)$$

In eq.A.4, R_{dis} is the radius of the cap beyond which H_2 dissociates, that we have measured both from the 2.122μm (Figure 13) and 1.644μm emission contours (Figure 14). Both of them give $R_{dis} \sim 20$ pixels. We also have estimated $v_{bow} = 115\pm5$ km s^{-1} from the FWZI of the 1.644μm (Hartigan, Raymond & Hartmann, 1987). Substituting these values in eq.A.4, we b as a function of v_{dis} only, that we have taken as a free parameter.

The above expression of b is then substituted in the parabolic equation to derive z_{max}:

$$z_{max} = \frac{b}{2}\left[\left(\frac{v_{bow}}{v_{max}}\right)^2 - 1\right] = \frac{b}{2}\left[\frac{1}{\sin\theta_{max}^2 - 1}\right] \qquad (A.5)$$

Following Hartigan, Raymond & Hartmann (1987) and considering that the bow is seen from the back (D99), we get $\theta_{max} = \pi/2 - \alpha/2$. Thus:

$$z_{max} = \frac{b}{2}\left[\left(\frac{1}{\cos\left(\alpha/2\right)}\right)^2 - 1\right] \qquad (A.6)$$

In conclusion, from equations A.4 and A.6 and by measuring χ from simple geometrical considerations, we are able to express in eq.A.1 D$'$ as a function only of α and v_{dis}, that have been routinely varied to match our measurement of D$'$, as shown in Figure 15.